DESIGN OF DRIVER ELECTRONICS FOR 32 CANTILEVERS IN ATOMIC FORCE MICROSCOPY

A THESIS

SUBMITTED TO THE DEPARTMENT OF ELECTRICAL AND ELECTRONICS ENGINEERING

AND THE INSTITUTE OF ENGINEERING AND SCIENCES

OF BILKENT UNIVERSITY

IN PARTIAL FULFILLMENT OF THE REQUIREMENTS

FOR THE DEGREE OF

MASTER OF SCIENCE

By

Müjdat Balantekin

September 2001

I certify that I have read this thesis and that in my opinion it is fully adequate, in scope and in quality, as a thesis for the degree of Master of Science.

Prof. Dr. Abdullah Atalar (Supervisor)

I certify that I have read this thesis and that in my opinion it is fully adequate, in scope and in quality, as a thesis for the degree of Master of Science.

Prof. Dr. Hayrettin Köymen

I certify that I have read this thesis and that in my opinion it is fully adequate, in scope and in quality, as a thesis for the degree of Master of Science.

Assoc. Prof. Dr. Recai Ellialtıoğlu

Approved for the Institute of Engineering and Sciences:

Prof. Dr. Mehmet Baray
Director of Institute of Engineering and Sciences

ABSTRACT

DESIGN OF DRIVER ELECTRONICS FOR 32 CANTILEVERS IN ATOMIC FORCE MICROSCOPY

Müjdat Balantekin
M. S. in Department of Electrical and Electronics Engineering
Supervisor: Prof. Dr. Abdullah Atalar
September 2001

Atomic Force Microscope (AFM) is a powerful tool used for high resolution surface imaging. A cantilever with a sharp tip acts as the position sensor of the AFM. One cantilever is generally employed for most AFM operations, and this approach produces images of large samples very slowly. Imaging can be speeded up when a cantilever array in parallel is utilized. Since more than one cantilever is operated, an electronic system that automates the image acquisition should be designed. In this thesis, a printed circuit board is designed for 32 cantilevers. Three of them can be operated in parallel to drive 96 cantilevers. The design is suited to operate the microscope in contact mode. The other widely used mode is the vibrating cantilever mode in which the cantilever can be modelled as a damped harmonic oscillator. This model can be converted to an electrical circuit which can be simulated with an electrical circuit simulator. In this thesis, we also present the simulation results of the vibrating cantilever.

Keywords: Atomic Force Microscope, Cantilever Array, Printed Circuit Board, Contact Mode, Vibrating Cantilever.

ÖZET

ATOMİK KUVVET MİKROSKOBUNDA 32 KALDIRAÇ İÇİN ELEKTRONİK DEVRE TASARIMI

Müjdat Balantekin
Elektrik ve Elektronik Mühendisliği Yüksek Lisans
Tez Yöneticisi: Prof. Dr. Abdullah Atalar
Eylül 2001

Atomik Kuvvet Mikroskobu (AKM) yüksek çözünürlükte yüzey resimlemesi için kullanılan güçlü bir alettir. Sivri uçlu kaldıraç AKM'nin algılayıcısıdır. Çoğu AKM çalışmalarında bir kaldıraç kullanılır, ve bu yaklaşım büyük örneklerin resmini çok yavaş üretir. Resimlemenin hızı kaldıraç dizisinin paralel kullanılmasıyla arttırılabilir. Birden fazla kaldıraç çalıştırıldığı için, resim elde etmeyi otomatikleştiren bir elektronik sistem gereklidir. Bu tezde, 32 kaldıraç için bir baskılı devre levhası tasarlanmıştır. Bunlardan üç tanesi paralel çalıştırılarak 96 kaldıraç sürülebilir. Tasarım, mikroskobu temas modunda çalıştırmaya uygundur. Kaldıracın sönümlenen harmonik osilatör olarak modellenebildiği geniş ölçüde kullanılan diğer bir modda titreşen kaldıraç modudur. Bu model bir elektrik devresine dönüştürülüp simülasyonu yapılabilir. Bu tezde, ayrıca titreşen kaldıracın simülasyon sonuçları sunulmuştur.

Anahtar Kelimeler: Atomik Kuvvet Mikroskobu, Kaldıraç Dizisi, Baskılı Devre Levhası, Temas Modu, Titreşen Kaldıraç.

ACKNOWLEDGMENTS

I would like to thank my supervisor Prof. Dr. Abdullah Atalar for his supervision, guidance, and suggestions throughout the development of this thesis.

I would also like to thank Dr. G. Göksenin Yaralıoğlu for helpful discussions and comments on the design.

Special thanks to Dr. Hayrettin Köymen and Dr. Recai Ellialtıoğlu for reading the thesis.

Contents

List of Figures

Chapter 1

INTRODUCTION

An Atomic force microscope [1] measures the interatomic forces between the tip attached to the cantilever and the sample. This sensitive device can also measure electrostatic, magnetic, and friction forces as well. AFM has become a versatile and powerful tool for imaging and modification of a wide range of materials such as biomolecules, polymers, metals, and semiconductors. The three dimensional images have allowed scientists to see atoms, molecules, and other nanoscale topographical features with excellent accuracy and precision in ambient, vacuum, and liquid environments. The originators of the microscope reported a lateral resolution of 30 Å and a vertical resolution less than 1 Å.

The microscope can be operated in one of the three modes. These are contact mode, noncontact mode, and intermittent-contact mode (tapping mode). Contact mode is the most common method of operation of the AFM. Figure 1.1 shows a schematic overview of the operating principle of an AFM. A sharp tip mounted on a cantilever is brought in close proximity of a sample surface, giving rise to the emergence of a force between tip and sample. First the force is attractive, but when the tip to sample distance gets very small, the force becomes repulsive and grows steeply with decreasing distance as it is seen in Fig. 1.2. The forces acting on the tip will cause the cantilever to deflect. By

detecting this deflection one can infer the force acting on the tip. When the probe tip is dragged across the surface, the resulting three dimensional image is a topographical map of the surface of the sample. The contact mode is divided into two modes : constant force and constant height mode (see Fig. 1.3). If the electronic feedback is switched on, then the positioning piezo which is moving the sample (or cantilever base) up and down can respond to any changes in detected force, and alter the tip-sample separation to restore the force to a predetermined value. An increase in the force due to raised surface features causes the feedback electronics to lower the sample away from the tip. A decrease in force due to a pit on the surface causes the sample to be raised towards the tip to keep the force constant. This mode of operation is known as constant force mode where the AFM not only measures the force on the sample but also regulates it, allowing acquisition of images at low forces. In constant force mode, the speed of scanning is limited by the response time of the feedback circuit. If the feedback electronics are switched off, then the microscope is said to be operating in constant height mode. This is particularly useful for imaging very flat samples at high resolution. In the constant height mode the sample height is fixed during scanning. Raised features on the sample surface cause an increase in the tip-sample force and this directly correlates to the height of the sample at that point. The constant height mode is also essential for recording real-time images of changing surfaces, where a high scan speed is essential. Contact mode AFM has been used extensively to image large samples, e.g., computer hard disks, CDs, etc., because it is the fastest operating mode. But the high lateral shear forces result in a tip wear so that frequent tip change is needed. To alleviate this problem, special hardened tips are used in contact mode AFM, but the hardened tips scratch the sample surface.

Tapping mode is the next most common mode used in AFM. The cantilever is oscillated at or near its resonant frequency and positioned above the surface so that it only taps the surface for a very small fraction of its oscillation period. The energy of the cantilever is large enough to avoid sticking of the tip to the sample surface. The primary advantage of tapping mode is that lateral forces can be eliminated between the

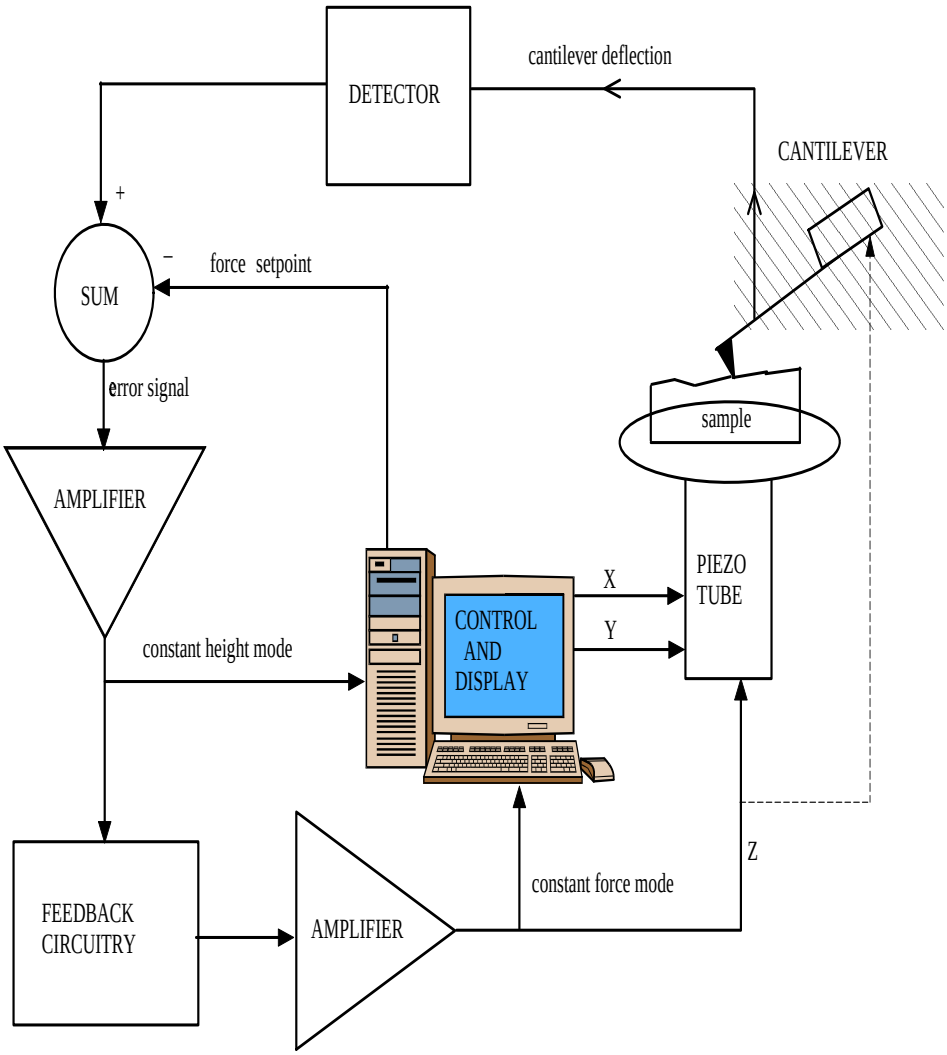

Figure 1.1: Schematic AFM setup.

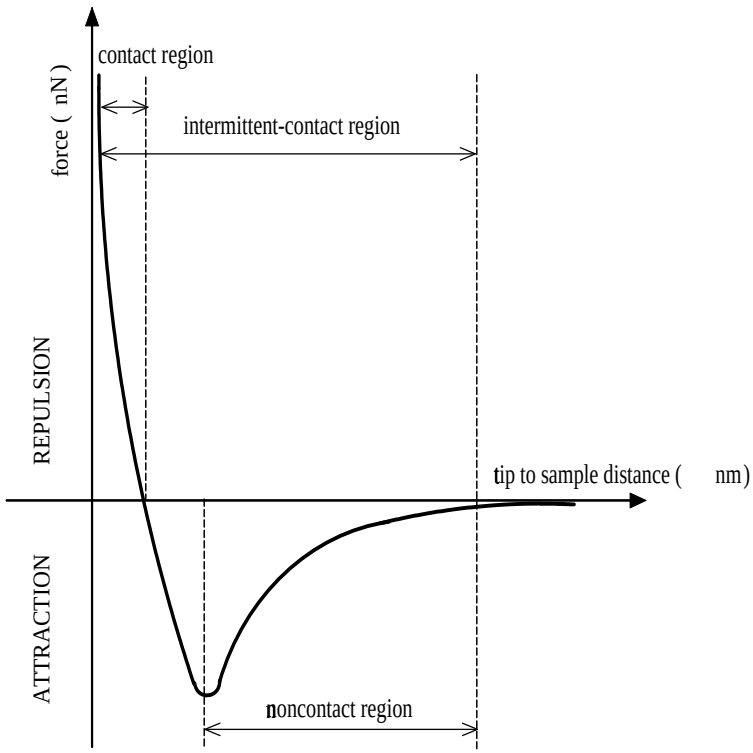

Figure 1.2: Intermolecular force versus distance curve.

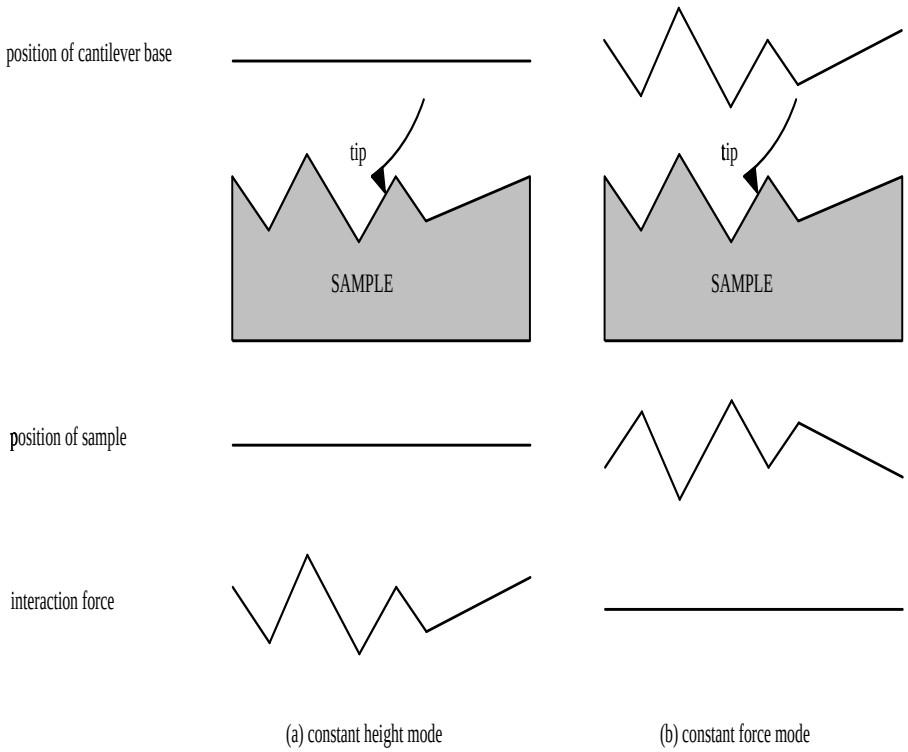

Figure 1.3: Contact mode operation. (a) Constant height, (b) Constant force.

tip and sample, which greatly reduces the force imparted on the sample and improves image resolution. In this mode, the amplitude or the phase of the cantilever vibration is used for feedback. Usually, the tapping mode is operated in a constant amplitude mode, i.e., the oscillation amplitude is adjusted until the feedback set point amplitude is reached. As far as structural properties of a surface are concerned, the phase shift yields information comparably to the changes in the amplitude. Recording the difference between the phase angle of the excitation signal and the tip oscillation could be applied for performing compositional maps and for imaging material properties such as stiffness and viscoelasticity. When imaging soft samples, tapping mode may be a better choice than contact mode for imaging.

Noncontact operation is another method which may be employed when imaging by AFM. The cantilever must be oscillated above the surface of the sample at such a distance

that the tip is no longer in the repulsive regime. Attractive van der Waals (vdW) forces acting between the tip and the sample are detected, and topographic images are constructed by scanning the tip above the surface. This is a very difficult mode to operate in ambient conditions with the AFM. The thin layer of water contamination which exists on the surface of the sample will invariably form a small capillary bridge between the tip and the sample and cause the tip to jump to contact with sample. Noncontact mode provides substantially lower resolution than either contact or tapping mode.

There are several deflection detection methods used in AFM. The detector used to measure the deflection of the cantilever is crucial in determining the performance of the microscope. The widely used detectors are based on tunneling, interferometry, optical lever, capacitance, and piezoresistor. Except piezoresistive sensing method [2], all other schemes need sensing element external to the cantilever. Therefore they require alignment to the cantilever, which must be maintained during scanning. In our design piezoresistive sensing method is used.

The operation principle of the piezoresistive detection method is very simple. Silicon exhibits a strong piezoresistive effect and it is a suitable material for fabricating cantilever beams. The resistance of the piezoresistor changes when the cantilever is stressed with deflection. A deflection results in a resistance change. A Wheatstone bridge can be used to convert the resistance change into an electrical signal. Figure 1.4 shows the schematic diagram of the piezoresistive detection scheme for AFM. The detected voltage is linearly proportional to the resistance change which is linearly proportional to cantilever deflection. The minimum detectable deflection of the cantilever, i.e., the vertical resolution of the microscope is determined by the sensitivity and the noise in the system. The sensitivity is the resistance change per unit deflection. The fundamental noise is the Johnson noise in the piezoresistor. A vertical resolution of 0.1 Å_{rms} was achieved using this technique [2]. Lateral resolution depends on the tip radius which is typically less than 50 nm.

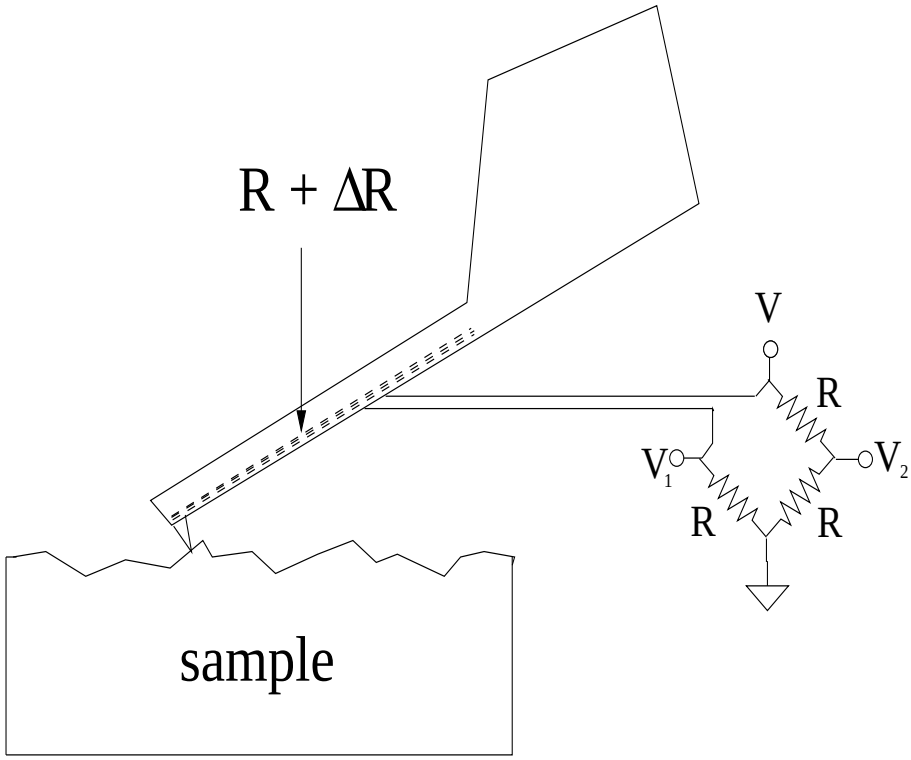

Figure 1.4: Piezoresistive detection scheme.

One of the limitations of constant force contact mode AFM is its relatively slow scan speed because of the poor mechanical response of piezotubes used to scan a sample. Materials are imaged with AFM in a production environment for quality control. Speed of measurement is critical ; the faster the measurement, the higher the production throughput. Operation in constant height contact mode is faster, however only very hard samples can be imaged in this mode. An alternative solution was proposed by Minne *et al.* [3] who operated two cantilevers in parallel and recorded two AFM images at the same time. The cantilevers that they used contained both an integrated piezoresistive silicon sensor and integrated piezoelectric zinc oxide (ZnO) actuator. A vertical resolution of 22 Å was reported. The piezoresistive sensor is used to detect the strain and provide the feedback signal for the ZnO actuator. Individual control of the tip-sample spacing is achieved with piezoelectric actuators. One problem of this technique is the electrical crosstalk between the ZnO signal and the piezoresistor signal since the actuator and sensor are integrated on the same cantilever. It was found that the problem of electrical coupling can be solved by measuring the response of the piezoresistor with a lock-in amplifier [4]. Although this technique significantly increased the imaging speed, its imaging bandwith was limited by the detection electronics rather than the mechanical resonance of the cantilever. By using an integrated actuator and optical lever sensor imaging bandwith was increased from 6 kHz to 33 kHz [5]. But this method did not take the advantage of parallel operation of cantilever array. The same group fabricated an array of 50 cantilevers which are spaced by 200 μm with eliminating capacitive coupling between the actuator and the sensor [6]. They achieved 20 kHz imaging bandwith with vertical resolution less than 50 Å. Hence the throughput of the AFM is increased both by parallel operation of cantilevers and enhanced tip speed. All these studies resulted in millimeter scale images much larger than typical AFM images [7]. However operating more and more cantilevers in parallel increases the amount of data to be processed and slows down the operation.

This thesis is composed of two parts. In the first part, we analyze the dynamics of

vibrating cantilever by using an electrical circuit simulator. We give the model of the tip-sample system and present the simulation results. In the second part, we advance the parallel operation of the cantilever array by designing an electronic system which is capable of driving 96 cantilevers. We show a detailed description of the system where contact mode is the operating mode of AFM. The conclusions are presented in chapter 4.

Chapter 2

SIMULATIONS OF VIBRATING CANTILEVER

In contact mode the tip is brought into close contact with the sample and the deflection of the tip is detected. This mode is stable and gives the highest resolution but has a drawback that the strong repulsive forces may damage soft samples and the tip. In vibrating cantilever mode the tip oscillates at or near its resonance frequency above the surface. In this case, the amplitude or the phase of the vibrating cantilever is used for feedback. Depending on the free oscillation amplitude it is called either noncontact or intermittent contact mode. Noncontact AFM is primarily used for imaging very soft materials. One of the most important problem in this mode is that the resolution is limited to the scales on the order of the tip-sample separation [8]. Since the amplitude is small, the tip can be captured by the sample. Immersing the tip and the sample in a liquid is suggested so that the negative Hamaker constant results in repulsive vdW forces which prevent the tip to jump into contact with sample [9]. In the tapping mode the amplitude is larger than that of the noncontact mode such that both attractive and repulsive force regions may be entered. Although there is a behavioral description [10] of the two modes one can not distinguish them by just considering amplitude damping

in the absence of phase data. In fact, operating the microscope in one of these states is an important issue for phase imaging since the same material shows different responses for each mode.

There are several studies [11–13] discussing the dynamics of the vibrating tip. All of them reported step-like discontinuity called "switch point" in the amplitude versus distance curves both experimentally and theoretically. Kühle [13] and Garcia [11] reported imaging artifacts due to the transition from the low oscillation state to the high oscillation state or vice versa. Although the damping, switching and hysteresis in amplitude and phase curves are observed in experiments, a clear explanation of these phenomena does not exist. In order to interpret the experimental data correctly, we must have a good model that can be easily simulated in the time domain.

2.1 Point-mass model

In a point-mass model, the tip is modelled as a forced oscillator and the sample is represented with a spring and a damper. This results in the following pair of differential equations:

$$m\ddot{z}_t + (mw_o/Q)\dot{z}_t + k_t(z_t - z_r) - f_{ts} = F_d\cos(wt)\ , \tag{2.1}$$

$$\gamma_s\dot{z}_s + k_s z_s + f_{ts} = 0. \tag{2.2}$$

where F_d and w are the amplitude and angular frequency of driving force, m, Q, w_o, k_t are the mass, quality factor, resonance frequency and spring constant of the cantilever, respectively. γ_s and k_s are the damping coefficient and stiffness of the sample. The mass of the sample is ignored. The derivatives are taken with respect to time. z_r is the rest position of the tip above the sample. z_t and z_s are the positions of the tip and sample, respectively. Interaction force, f_{ts}, can be approximated as a function of tip to sample distance, d, by [14]:

$$d_o = \sqrt[6]{\frac{\sigma}{30}}\ , \tag{2.3}$$

$$f_{ts}(d) = \frac{HR}{6\sigma^2}\left[-\left(\frac{\sigma}{d}\right)^2 + \frac{1}{30}\left(\frac{\sigma}{d}\right)^8\right] \qquad d > d_o\ , \tag{2.4}$$

$$f_{ts}(d) = \frac{8\sqrt{2R}}{3\left[\frac{1-v_1^2}{E_1} + \frac{1-v_2^2}{E_2}\right]}(d_o - d)^{1.5} \qquad d \leq d_o. \tag{2.5}$$

where H, R, σ, E_i, and v_i are the Hamaker constant, radius of the tip, interatomic distance, Youngs modulus, and Poisson coefficient, respectively. The mechanical model is depicted in Fig. 2.1(a).

A novel method [15] is proposed to simulate the tip-sample system. One can replace masses with inductors, springs with capacitors, dampers with resistors, and forces with voltages. We can then rewrite the original pair of differential equations as follows

$$L_t\ddot{q}_t + R_t\dot{q}_t + q_t/C_t - f_{ts} = F_d\cos(wt) + V_o\ , \tag{2.6}$$

$$R_s\dot{q}_s + q_s/C_s + f_{ts} = 0. \tag{2.7}$$

where the charges of the capacitors, q_t and q_s, represent the position of the tip and sample with respect to reference point. The equations define an equivalent electrical circuit shown in Fig. 2.1(b). We can simulate this circuit with a powerful electrical simulator such as HSPICE^{TM} to find tip-sample interactions.

2.2 Simulations

For the simulations driving frequency is set to resonance frequency of the cantilever. The peak to peak free oscillation amplitude of the cantilever is 25 nm. The cantilever parameters are chosen to be $k_t = 10$ N/m, $Q = 250$, $f_o = 15.9$ kHz with 100 nm tip radius. The value of tip radius is chosen such that Eq. (2.4) is valid [16]. It is assumed that the damping constant of the sample is low and the Youngs modulus of the tip is larger than that of the sample. The relation between the spring constant of a material and elastic modulus of a material and the maximum force exerted on sample is given in

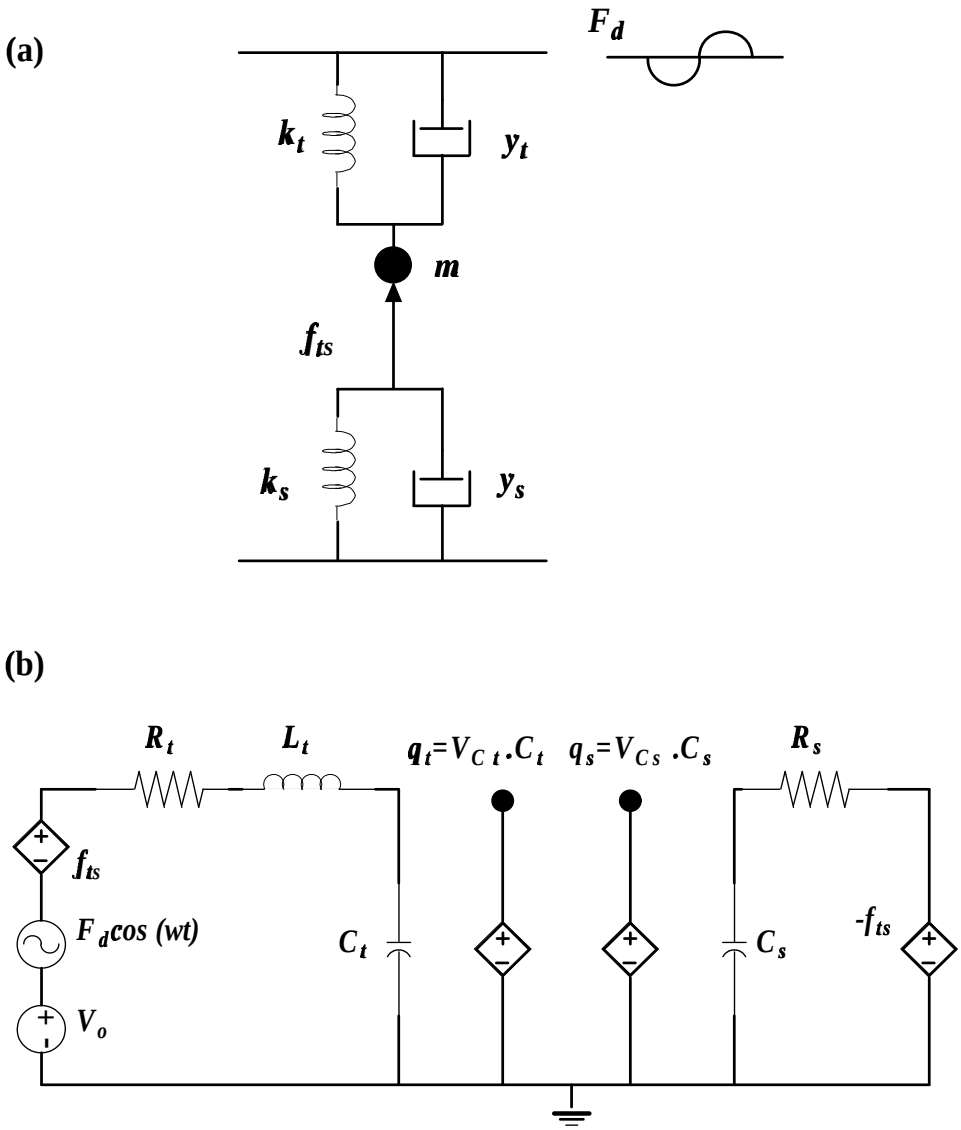

Figure 2.1: (a) The mechanical model for tip-sample system. (b) Equivalent electrical model. t stands for tip, s stands for sample.

the literature [17]. When simulations are performed the tip approaches or retracts from the sample with a speed of 10 nm/s.

Figure 2.2 shows the amplitude and phase versus distance curve for a sample spring constant of 25 N/m. When the tip approaches the sample, the oscillation amplitude is damped as a result of the interaction forces that exists between the tip and the sample. In the absence of the phase data we can not say whether it is attractive or repulsive damping. By looking at the phase difference between the tip and the driving force we can conclude that for attractive damping where the tip is in the noncontact regime the phase shift is more than 90^o. While the tip is in tapping mode the phase shift is less than 90^o and repulsive damping occurs.

While the tip oscillates above the sample, interaction forces are created. In order to analyze the damping mechanism we need to find these forces. Figure 2.3 shows the force traces taken from simulations for $k_s = 25$ N/m. These traces together with the phase curve shown in Fig. 2.2(b) explain damping and switching mechanisms. Figure 2.3(a) to (d) is taken when tip approaches the sample while (e) to (g) correspond to retract cycles. Their corresponding places are indicated in Fig. 2.2.

While the cantilever is oscillating freely (in the absence of interaction forces) there is a 90^o phase difference between the driving force, $\mathbf{F_d}$, and tip oscillation. From now on boldface symbols represent the phasors. In Fig. 2.3(a) tip to sample distance is 15.6 nm and the small pulses are the attractive forces. If we take the Fourier series of these pulses by setting the reference point such that the tip oscillation is a cosine then due to even symmetry the resultant first harmonic is also a cosine. That means the first harmonic of the force is in-phase with the tip oscillation, $\mathbf{V_{tip}}$. In addition to the driving force we now also have the first harmonic of the interaction force, $\mathbf{F_{ts1}}$. The combination of them must have a 90^o phase shift with respect to tip oscillation. These two constraints make the amplitude decrease. This situation is explained in Fig. 2.4 which shows the trajectories of tip oscillation, first harmonic of interaction force, and total force. A phasor diagram

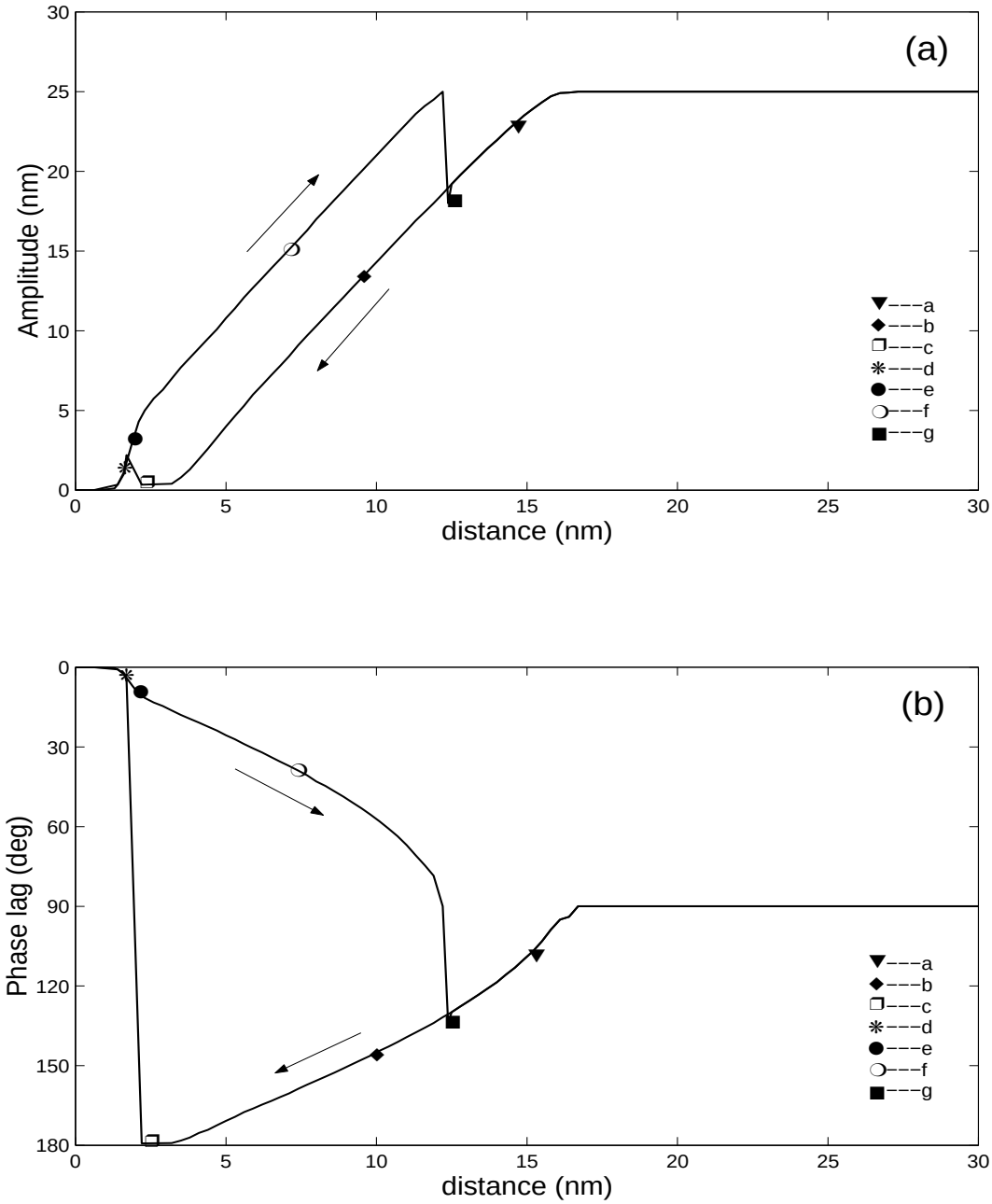

Figure 2.2: Amplitude and phase versus distance simulation results at resonance frequency for $k_s = 25$ N/m. (a) Amplitude, (b) Phase lag. Markers show the positions where the force traces in Fig. 2.3 are taken.

is also given for this condition. $\mathbf{F_d}$ has an amplitude of 0.5 nN and phase of 0^o. The markers from a to g correspond to same markers in Fig. 2.2. Since the combined force has a smaller amplitude and since the tip oscillation amplitude is proportional to this force, the oscillation amplitude decreases. With a decreasing tip to sample spacing, the amplitude of the negative going pulses increases as shown in Fig. 2.3(b). If we look at Fig. 2.4 again, $\mathbf{F_{ts1}}$ is in-phase with $\mathbf{V_{tip}}$ and the amplitude continues to decrease as the total force decreases. Figure 2.3(c) shows the forces almost become a cosine with a 177^o phase shift with respect to $\mathbf{F_d}$ so that the tip oscillation amplitude is very small. Figure 2.3(d) shows clearly the transition from the attractive regime to the repulsive regime. Since there is a transient term that modulates this amplitude, we take the steady state value. It is assumed that the steady state is reached after 200 oscillation cycles. In Figure 2.4 the marker d shows the situation after the transition in approach cycle. This time $\mathbf{F_{ts1}}$ is out of phase with $\mathbf{V_{tip}}$ but 90^o phase shift constraint again makes the oscillation amplitude decrease.

While retracting the tip, first there is a fast amplitude increase. If we look at Fig. 2.3(e), we can see that the positive going pulses crosses over the zero point which causes a first harmonic reduction. In Fig. 2.3(f) tip to sample distance is 7.4 nm. The forces are almost even symmetric and the first harmonic is out of phase with $\mathbf{V_{tip}}$. Corresponding situation is indicated with marker f in Fig. 2.4. The tip oscillation amplitude continues to increase up to a critical point where $\mathbf{F_{ts1}}$ becomes zero. At the critical point, a transition in retract cycle occurs. This situation is shown in Fig. 2.3(g). Actually the point where $\mathbf{F_{ts1}}$ becomes zero is before this time interval. The time axis is zoomed to show how transition takes place. After this switch point $\mathbf{F_{ts1}}$ again becomes in-phase with $\mathbf{V_{tip}}$ as shown in Fig. 2.4. It is important to note that this switch point depends highly on the initial conditions. If the system is started to oscillate with different initial conditions its position may change.

We obtain amplitude and phase curves for different material spring constants.

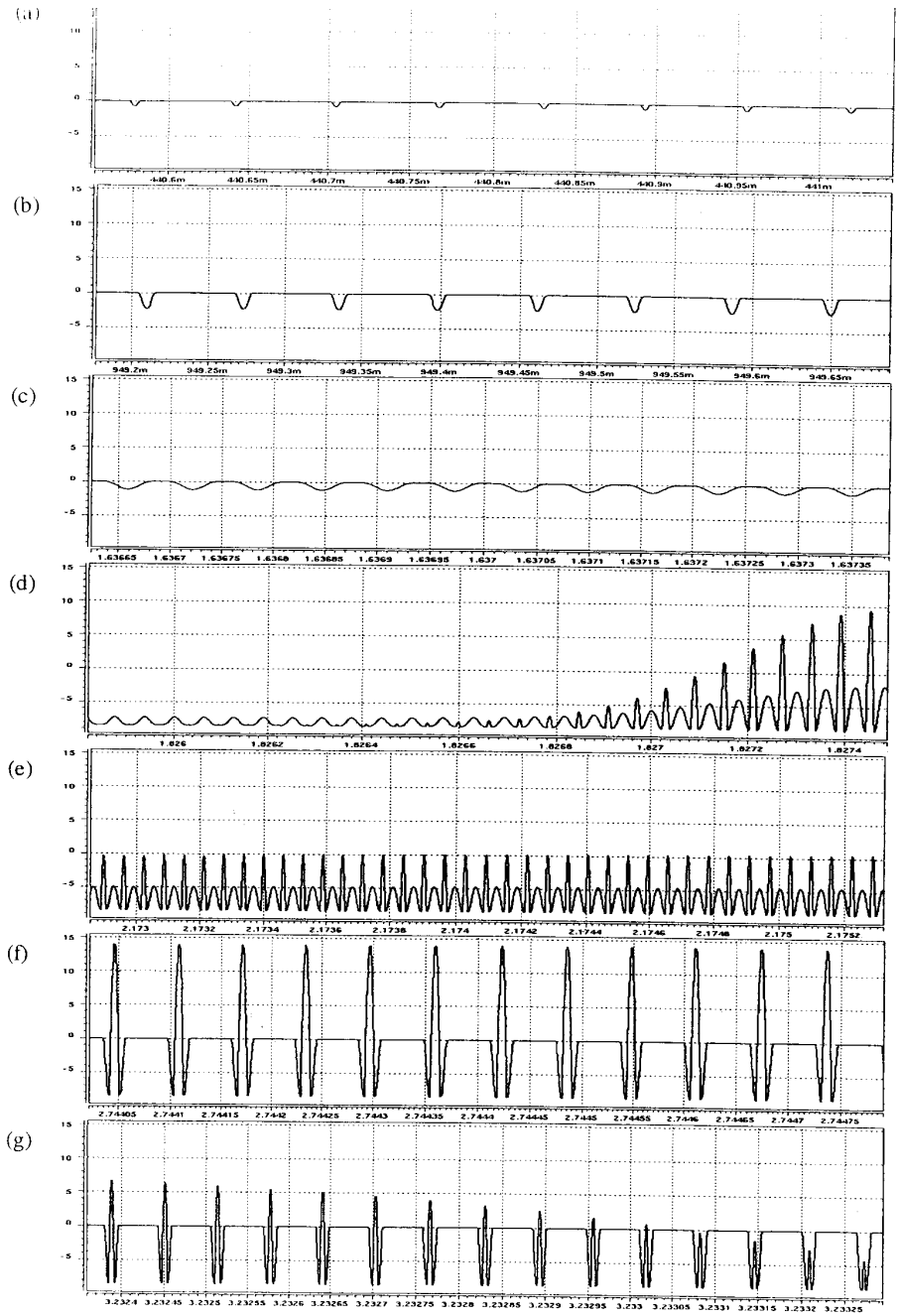

Figure 2.3: Interaction forces (nN) versus time (s) traces taken from simulations for $k_s = 25$ N/m. (a) to (d) corresponds to approach cycles. The tip to sample distance for (a) is the largest one and for (d) is the smallest. (e) to (g) corresponds to retract cycles. The tip to sample distance for (e) is the smallest one and (g) is the largest.

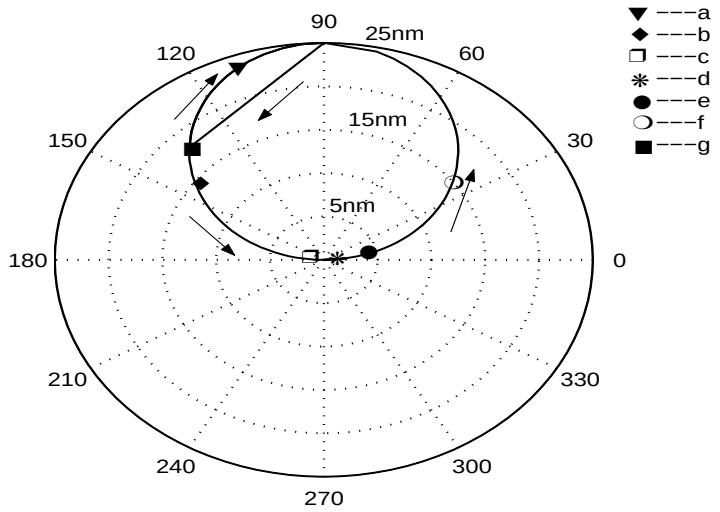

(a) Tip oscillation (Vtip)

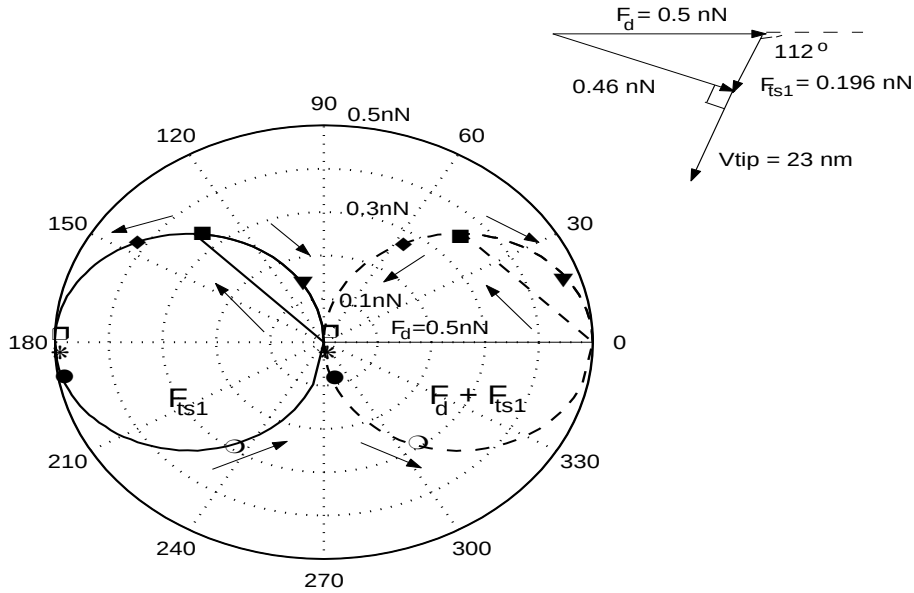

(b) First harmonic of interaction force (F_{ts1}) and total force ($F_d + F_{ts1}$)

Figure 2.4: Trajectories of (a) tip oscillation, (b) first harmonic of interaction force, and total force for $k_s = 25$ N/m. Solid line shows $\mathbf{F_{ts1}}$ and dashed line shows $\mathbf{F_d + F_{ts1}}$. Each marker corresponds to same marker in Fig. 2.2(b). The phasor diagram shows the situation indicated with marker *a*.

Figure 2.5 shows two of them: one is softer ($k_s = 2.5$ N/m) than the sample we have just described and the other is stiffer ($k_s = 250$ N/m). It clearly indicates that for stiff samples we have a large hysteresis which is not desired in normal operating conditions, but may be used for differentiating two samples with different elastic properties. However for compliant materials we see more damping since the surface deformation is more and there is negligible hysteresis. While the material gets softer and softer, the slope of the amplitude curve increases. Hysteresis for hard surfaces is formed due to state transitions which indicate a sign change of the force gradient. This effect makes it impossible to use vibrating cantilever mode at resonant frequency for a wide range of materials. This is because of the fact that the same oscillation amplitude can be reached for two different tip to sample distances for any given set point amplitude. One solution to this problem is to change the oscillation frequency [18, 19]. Another solution is change the free tip oscillation amplitude. The simulation results for peak to peak amplitudes of 100 nm and 5 nm is given in Fig. 2.6 and Fig. 2.7. It is seen that for 100 nm amplitude the tapping mode is enhanced. By selecting a proper set point amplitude the feedback ensures the microscope to operate safely in tapping mode. So the tapping mode is more stable than noncontact mode for this material. Decreasing the oscillation amplitude is not a good choice, since it creates the possibility of switching between noncontact and tapping modes. For very soft materials tapping mode is hard to achieve since the sample surface is pulled up easily by the tip. This makes the tip amplitude vanish, and the microscope generally operates in noncontact mode. However for relatively stiff materials higher repulsive forces causes the tip to go into tapping state. In conclusion, for stiff materials it is better to choose high oscillation amplitudes.

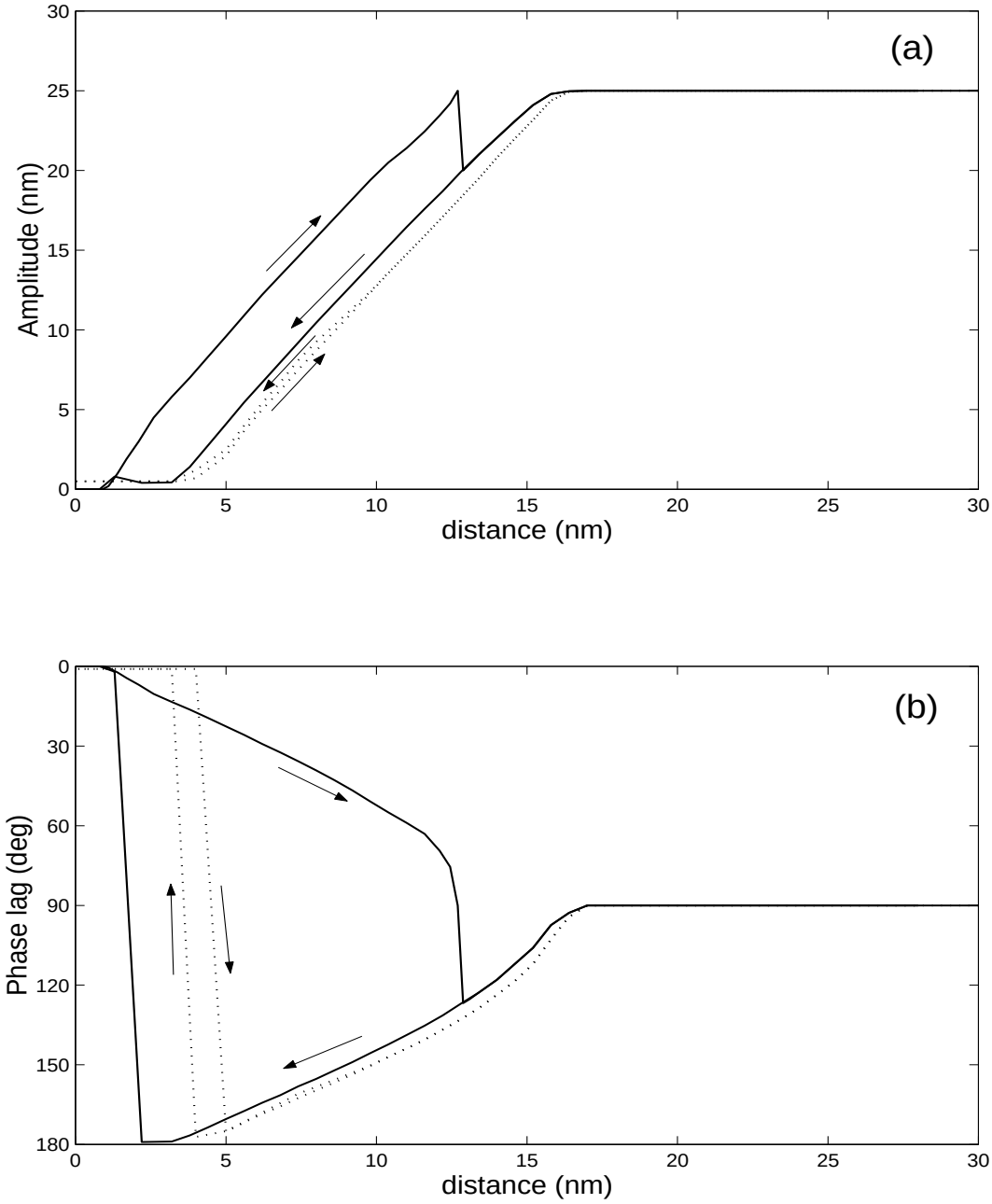

Figure 2.5: Amplitude and phase versus distance simulation results at resonance frequency for $k_s = 2.5$ N/m (dotted lines) and for $k_s = 250$ N/m (solid lines). (a) Amplitude, (b) Phase lag.

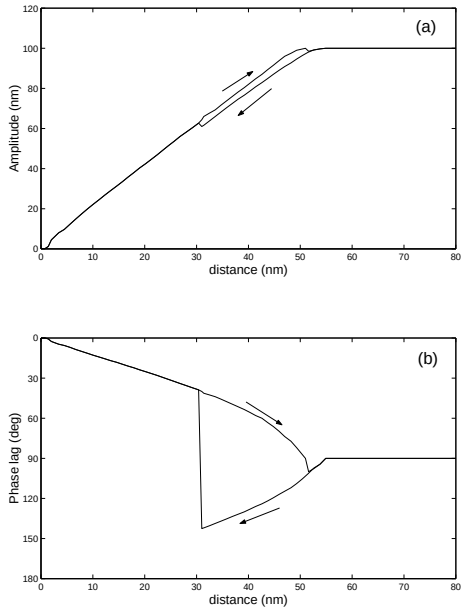

Figure 2.6: Amplitude and phase versus distance simulation results at resonance frequency for $k_s = 25$ N/m. (a) Amplitude, (b) Phase lag. The free tip oscillation amplitude is 100 nm.

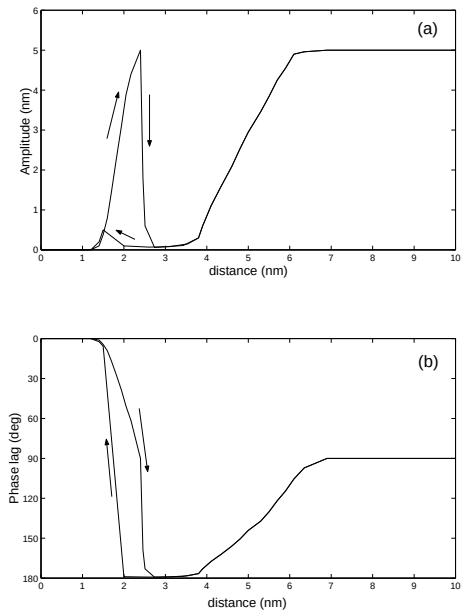

Figure 2.7: Amplitude and phase versus distance simulation results at resonance frequency for $k_s = 25$ N/m. (a) Amplitude, (b) Phase lag. The free tip oscillation amplitude is 5 nm.

Chapter 3

DRIVER ELECTRONICS FOR 32 CANTILEVERS

Atomic Force Microscope detects the surface features in nanometer scale. An electronic system is used to convert the height level of the sample to an electrical signal and hence to data bits. Also it gives the feedback signal to the actuator. The design of driver electronics depends on the detection scheme. In piezoresistive detection scheme, the deflected cantilever results in voltages at microvolt range [20]. The vertical resolution is determined by how well we detect this signal. Therefore we need a low noise electronic system used for amplification of the detected signal. It must also have high gain. In constant force mode, the feedback is switched on. By selecting wide bandwith operational amplifiers we can increase the phase margin and thus increase stability. The feedback should be fast enough to be able to keep track of the sample topography. Another issue is to occupy less space to make the board feasible. This needs multi-layered board with efficient placement and routing. The input and output traces should be narrow and as short as possible to reduce any stray capacitance on the PCB. Further reduction can be realized by choosing smaller footprint integrated circuits, and using a PCB material with a low dielectric constant. Some ICs have digital parts that can be controlled via PC

parallel port. The digital noise that is introduced at the ground pin could couple into the analog output. Therefore the digital circuitry should be isolated from the analog one. In the guide of these specifications we designed a 40×50 cm^2 electronic board whose parts are described in the following sections. It has four signal layers, four power planes, and it has more than 2500 components. The board accomodates 32 channels. A block diagram of one channel is shown in Fig. 3.1. The PCB layout is given in Appendix A and the component list is provided in Appendix B. Three boards can be operated in parallel to drive 96 cantilevers as shown in Fig. 3.2.

3.1 I/O Connectors and power supply

There are five connectors on the board. First two, which are used for cantilever array and ZnO actuators, are subdivided into two groups each containing 16 channels. So there are four 767054-1 multi pin coaxial MICTOR [21] connectors used to get input signal from the cantilevers and to carry output signal to the actuators. The third connector, 748483-5 AMPLIMITE [21], is used to take the filtered analog signal out of the board and connect it to another card, ICS-645 [22]. This card contains 32 16-bit A/D converters (AD9260 [23]). It supports a 33 MHz, 32-bit Master/Slave PCI interface. The parallel port connector is used to control the digital inputs of the ICs on the board with a PC. And the last connector is used for scanner. The lines of this connector are pulled up with 4.7 kΩ resistors to 5 V.

In any circuit where accuracy is important, careful consideration of the power supply helps to ensure the rated performance. There are three groups of power supplies for analog , digital, and high voltage section. Each group has its own ground. The ground path should be as wide as possible to reduce any effects of parasitic inductance and ohmic drops. Therefore a ground plane is used for each section. High voltage and analog grounds are connected at a single point on the board. The voltage regulators;

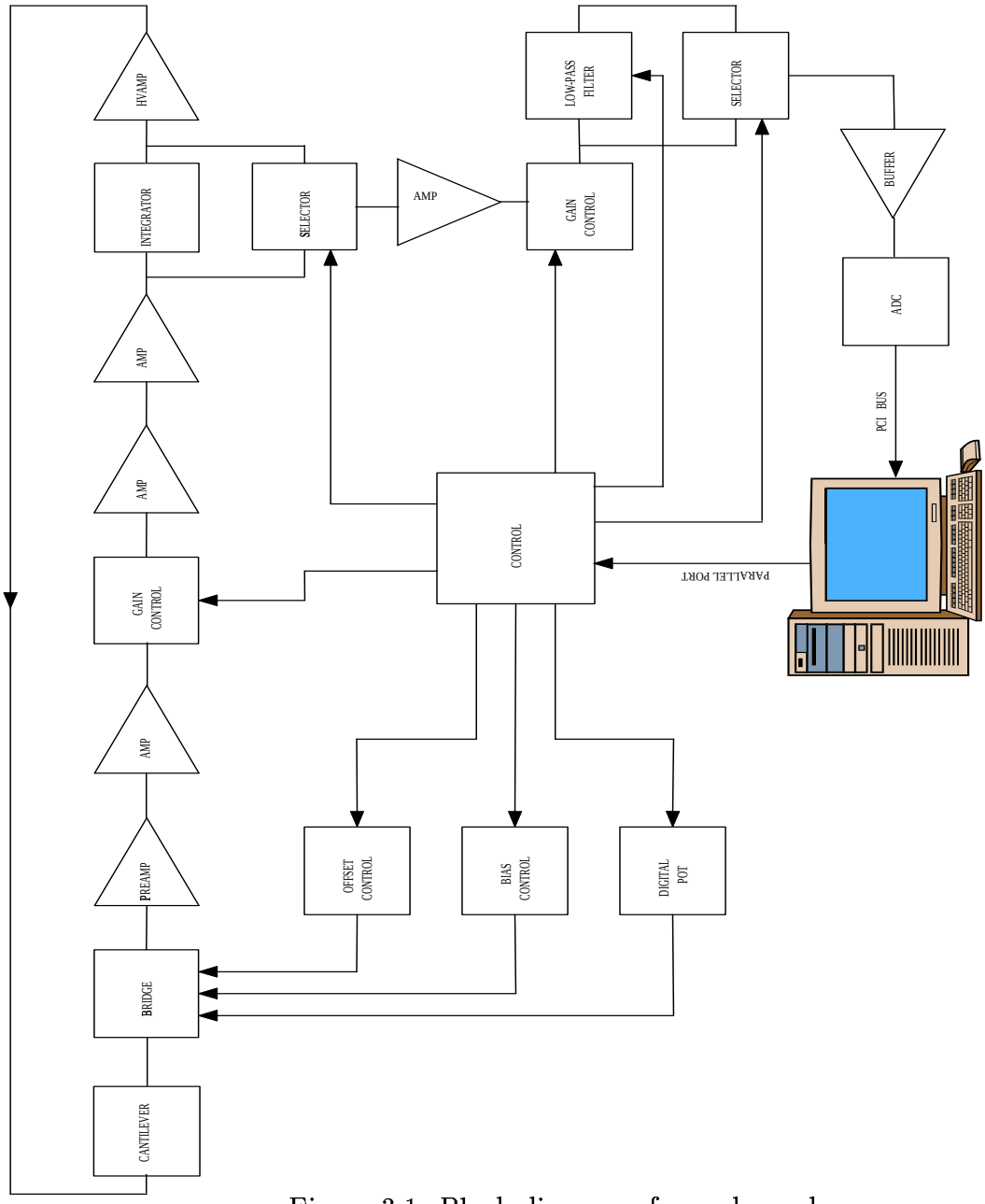

Figure 3.1: Block diagram of one channel.

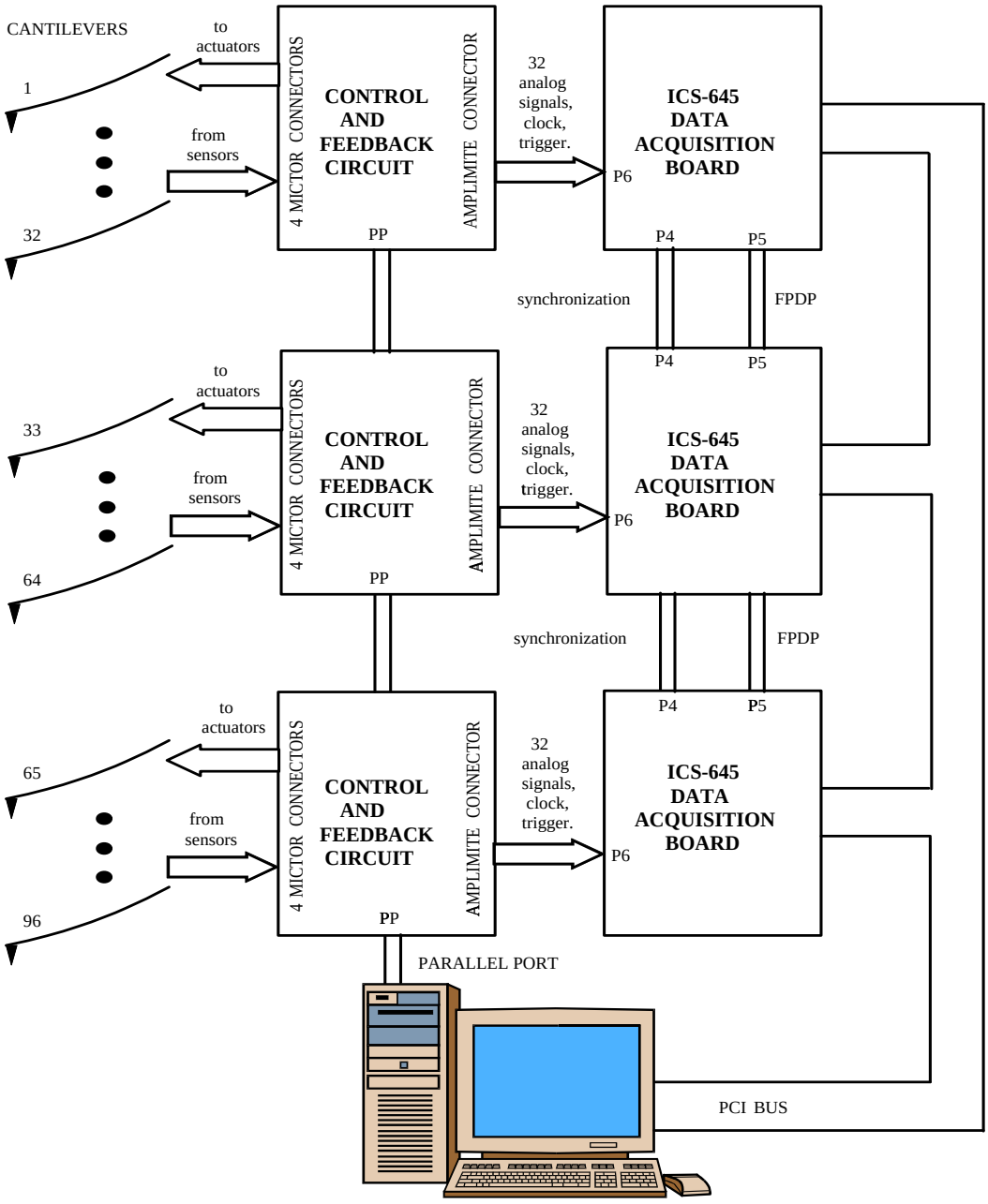

Figure 3.2: Parallel operation of 96 cantilevers.

LM317, LM2990, LM1086, LM2990, LM1085, and LM1086 [24] are used for +15 V, -15 V, +5 V analog, -5 V, +5 V digital, and +3.3 V supply voltages. Each regulator output is bypassed with 10 μF tantalum electrolytic and 0.1 μF ceramic chip capacitors. Supply pins of the ICs on the board are also bypassed with these capacitors. Tantalum capacitors are a good choice for their high capacitance/size ratio, but their effective series resistance increases with frequency making them less effective. On the other hand, the ceramic capacitor has low effective series resistance and inductance to provide a low impedance path to ground at high frequencies. Because of its small size, it can be placed very close to the device pin, further reducing the stray inductance. The high voltage power supply is regulated with a zener diode.

3.2 Wheatstone bridge and preamplifier

The Wheatstone bridge shown in Fig. 3.3 converts the resistance change in the cantilever to an electrical signal. The bias voltage is supplied with LM837 [24]. This is a quad package and one op amp drives four bridges. Two of them are used to supply the bias voltages of 32 bridges with $\pm$12.5 V output swing. It can drive a 600 Ω load making it suitable for our application. Its output is filtered with 0.1 μF and 10 μF capacitors. The input voltage of LM837 is adjusted by DAC8043 [25]. DAC8043 is controlled via 3-wire serial interface. REF02 [25] provides +5 V reference to DAC8043, hence the bridge bias voltage can be changed from 0 to +5 V with $5(1/2)^{12} = 1.2$ mV resolution. AD5204 [23] is a 4-channel, 256 position digital potentiometer. It is used to balance the bridge when there is no deflection. Eight of these devices are daisy chained to balance 32 bridges. DAC8420 [23] is a quad 12-bit voltage-output digital to analog converter, and is responsible for adjusting the force setpoint. Its output voltage range is determined by the reference voltages. AD588 [23], high precision voltage reference, is used for this purpose.

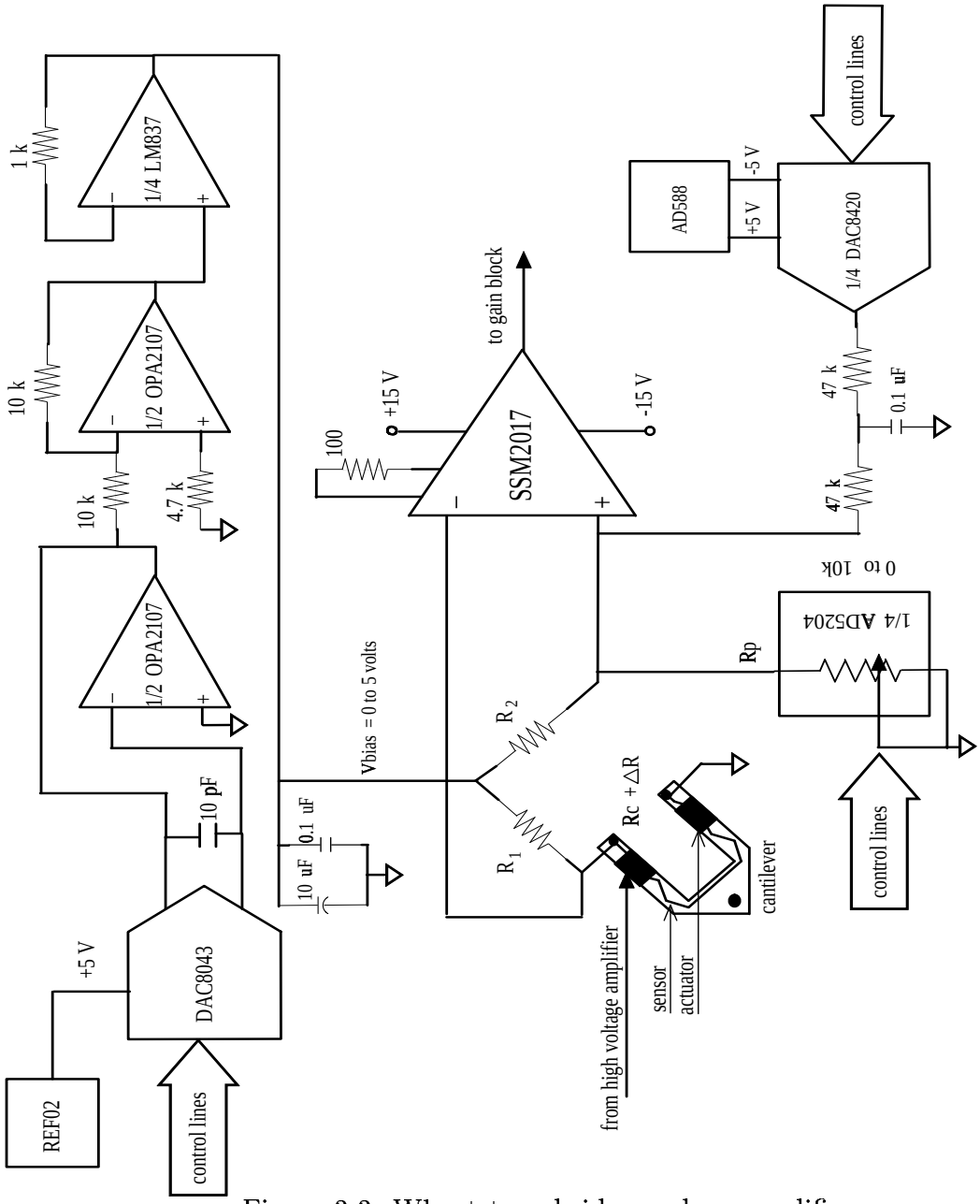

Figure 3.3: Wheatstone bridge and preamplifier.

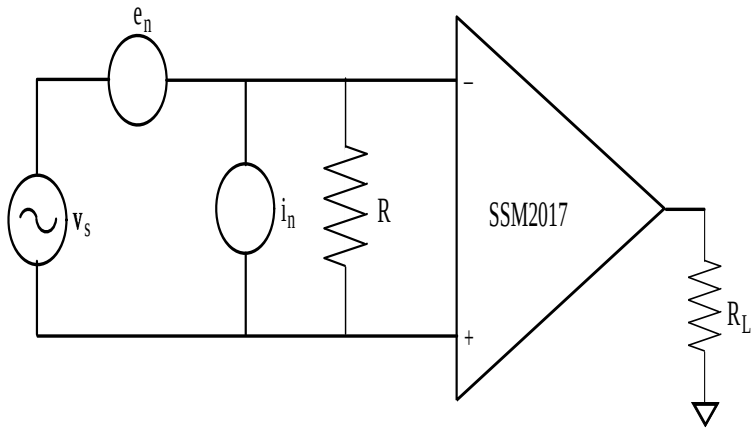

Figure 3.4: Equivalent noise circuit.

Excluding the mechanical noise of the cantilever, we have mainly four kinds of noise sources in the system. These are $1/f$ noise, Johnson noise, input noise voltage and input noise current of the amplifiers. Equivalent noise circuit is shown in Fig. 3.4 where $1/f$ noise is not included. The signal to noise ratio (SNR) is given by:

$$R = R_p \| R_2 + R_1 \| R_c \ , \tag{3.1}$$

$$SNR = \frac{V_{bias}^2 \left(\frac{\Delta R}{R_c}\right)^2 \left(\frac{R_p R_2}{(R_p+R_2)^2}\right)^2}{B(i_n^2 R^2 + e_n^2 + 4k_B T R)}. \tag{3.2}$$

where B is the bandwidth, i_n is the input noise current, e_n is the input noise voltage of SSM2017, k_B is the Boltzmann constant, T is the temperature. Resistance change per unit deflection is constant and depends on cantilever parameters.

In order to increase the SNR we have to use very low noise amplifier in the first stage of amplifier chain. SSM2017 [23] is an ultralow noise audio preamplifier used for this purpose. Its input voltage and current noise density are 1.95 nV/$\sqrt{\text{Hz}}$ and 2 pA/$\sqrt{\text{Hz}}$ at 1 kHz, respectively. It has a bandwidth of 1 MHz with a gain of 100 which is determined from external 100 Ω metal film resistor.

Increasing the bias voltage increases the output signal. However, $1/f$ noise increases as the bias voltage increases [2]. Also the power dissipated in the cantilever increases.

The maximum voltage applied to the resistor terminal of AD5204 can not exceed 5 V. So it is suitable to change the bias voltage between 0 and 5 V. Power dissipated on the cantilever is given by:

$$P_c = \frac{V_{bias}^2 R_p^2}{(R_p + R_2)^2 R_c}. \tag{3.3}$$

Minimum load that can be connected to LM837 output is 600 Ω. Since one op amp is loaded by four bridges, we can write,

$$(R_1 + R_c) \| (R_2 + R_p) \geq 2.4\ k\Omega. \tag{3.4}$$

For 1 mW power dissipation on cantilever, and 5 V bias voltage, the optimum resistor values and SNR are found to be: $R_1 = 4.8\ k\Omega$, $R_2 = 2.8\ k\Omega$, $R_c = 1.7\ k\Omega$, $R_p = 1\ k\Omega$,

$$SNR_{max} = 1.7643 \times 10^{16} (\frac{\Delta R}{R_c})^2 \frac{1}{B}. \tag{3.5}$$

In order to preserve the specified analog performance of the device, the supply should also be noise free as much as possible. The power pins of SSM2017 are bypassed with 0.1 μF and 10 μF capacitors (not shown in the figure). These capacitors are located as close to the package as possible.

3.3 Gain blocks

Since the detected voltage level is very low, we need a very high voltage gain. Excluding the voltage dividers, the overall loop gain can be adjusted from 0 to 337,500. The voltage dividers are used in order not to exceed maximum input voltage rating of the ICs. To do this we need variable gain attenuators and fixed gain amplifiers. To occupy minimal space on the board we use quad op amp packages and 8-channel DACs with 3-wire serial control interface. Figure 3.5(a) shows one of the gain block in the loop for one channel. It is constructed with one fourth of OP467 [23], high speed, precision op amp. This block has a gain of 15 with 2.5 MHz bandwidth. It can be operated either with ±5 V

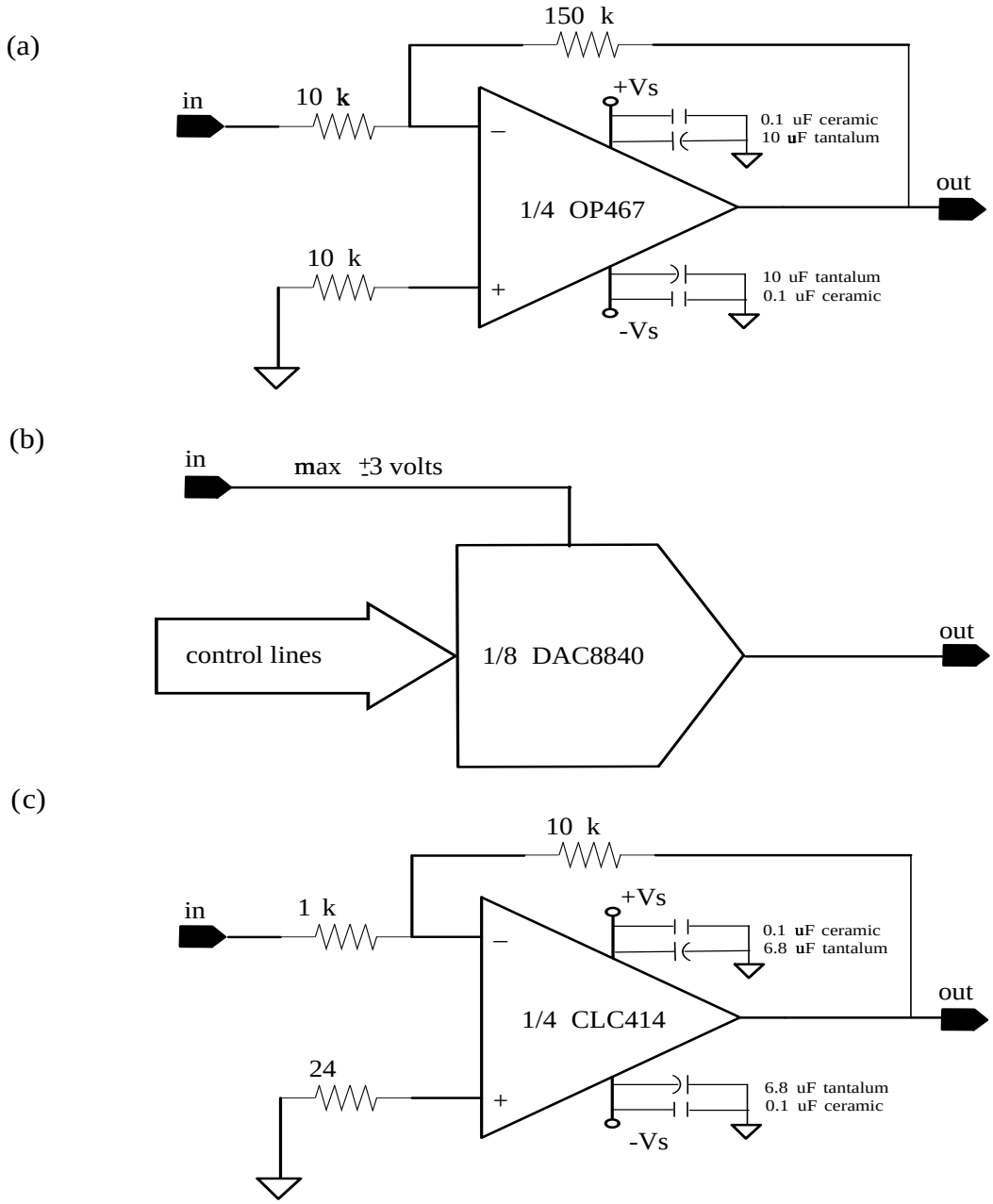

Figure 3.5: Gain blocks.

or ±15 V supply voltages. In this configuration, large resistors are chosen to minimize the output current of voltage regulators. Also external input bias current cancellation resistor is added. Although it increases the noise, at later stages noise becomes less important factor in the design.

DAC8840 [23] contains 8 voltage output CMOS digital to analog coverters, each with separate reference inputs. Each DAC has its own DAC register which holds its output state. These DAC registers are updated from an internal serial to parallel shift register which is loaded from a standard 3-wire serial input digital interface. Twelve data bits make up the data word clocked into the serial input register. This data word is decoded where the first 4 bits determine the address of the DAC register to be loaded with the last 8 bits of data. A serial data output pin at the opposite end of the serial register allows daisy chaining 4 chips to adjust the gain of 32 channels. The outputs of DAC8840 are buffered internally to drive up to 1 kΩ loads in parallel with 100 pF. Each channel provides a 1 MHz gain-bandwidth product where the gain can be adjusted from -1 to +1.

Figure 3.5(c) shows the second gain block used to control the gain of one channel with DAC8840. This block is used to control out of loop signals. CLC414 [24] is a low-power current feedback op amp which operates on ± 5 V power supply. The current feedback architecture has the advantage that the high slew rate allows the large signal performance to approach the small signal performance. Also its bandwidth is independent from the gain. However increasing the feedback resistor reduces the bandwidth as we did in order not to exceed the output current limit of DAC8840. A 24 Ω resistor to ground on the non-inverting input insures stability but does not provide bias current cancellation.

In any multi-channel integrated circuit there is an undesirable tendency for the signal in one channel to couple with and reproduce itself in the output of another channel or channels. This effect is referred to as crosstalk. In quad devices, the effect of crosstalk is measured by driving three channels and observing the output of the undriven channel over various frequencies. The magnitude of this effect is referenced in terms of channel to channel isolation and expressed in decibels. The channel isolations of OP467, DAC8840, and CLC414 are greater than 70 dB at 1 MHz.

3.4 Integrator

Integrator is used when the microscope is operated in constant force mode. In constant height mode it is deselected since there is no feedback. Time constant (RC) determines how fast the integrator's output responds to instantaneous changes in the input waveform. In order to minimize the overshoot and settling time we have to reduce the time constant. However reducing the time constant also reduces the stability of the control loop. It is therefore best to initially set the time constant as large as possible. Then it should be decreased until the system is still stable.

ADG662 [23], quad single pole single throw (SPST) switch, is used to reset the integrator. Its leakage current is less than 100 pA and is suitable for this purpose. It is normally open as shown in Fig. 3.6. ADG333A [23] is a quad single pole double throw (SPDT) switch and is used to select either input or output of the integrator.

3.5 High voltage amplifier

High voltage amplifier shown in Fig. 3.7 is used to drive ZnO actuator in constant force mode. For a given scan speed the imaging bandwidth is related to the response time of the feedback circuit. Therefore slew rate of the high voltage amplifier plays a key role and should be carefully considered in the design. PA98 [26] is a very high slew rate power amplifier and is recommended for our application. For a 10 pF compensation capacitance, its slew rate is 400 V/μs.

It can be operated from $\pm$15 V to $\pm$225 V supply voltages. Zener diode transient suppressors are used to protect the supply pins. We also used 0.1 μF metallized polyester film and 10 μF aluminum electrolytic capacitors on supplies. The compensation capacitor, 10 pF, must be rated at 500 V working voltage. An NPO capacitor is recommended. Low leakage, low capacitance JFETs (2N4416) connected as diodes are

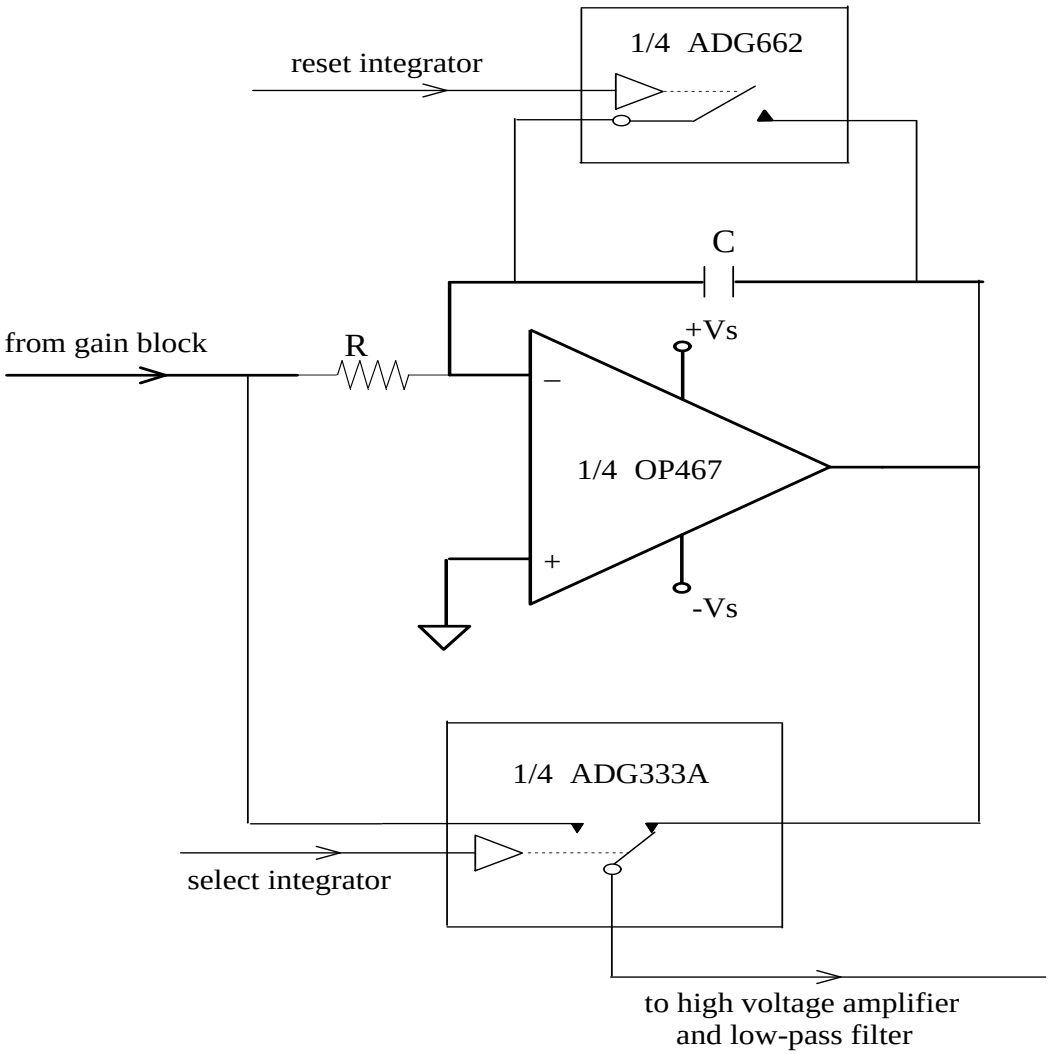

Figure 3.6: Integrator.

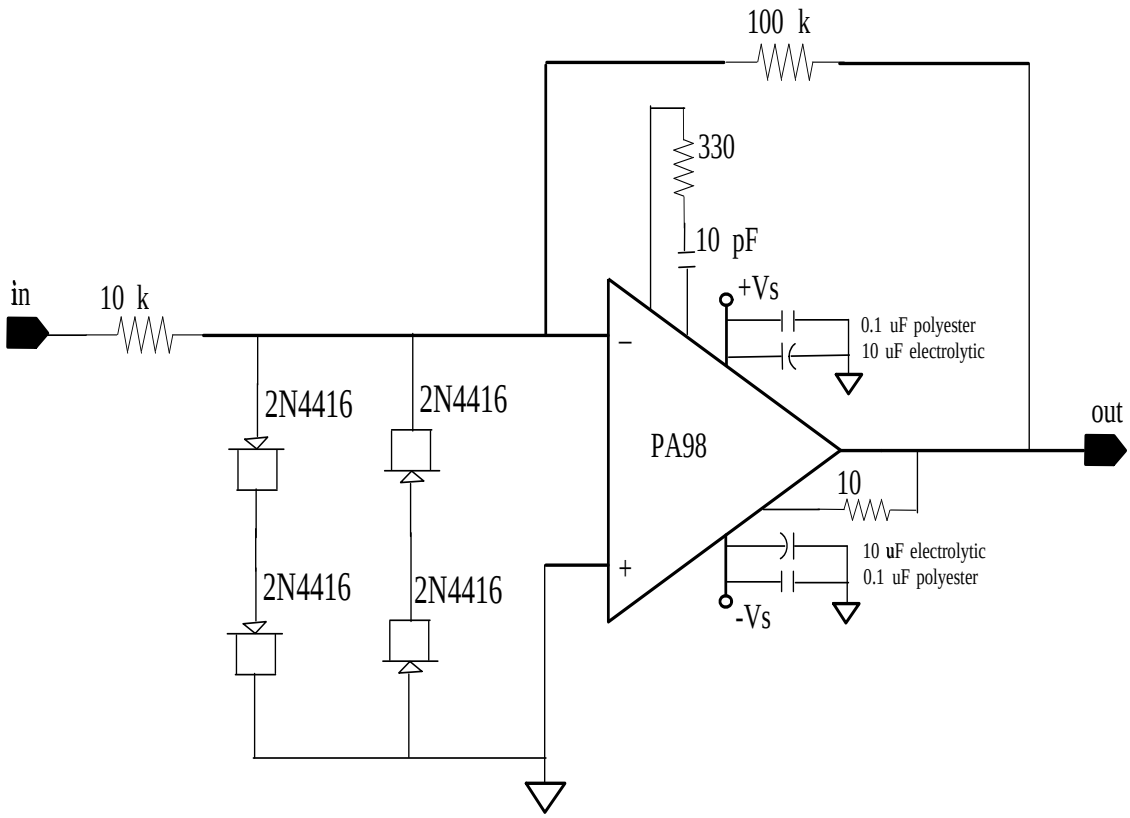

Figure 3.7: High voltage amplifier.

used to protect the input of PA98. The output current limit of the amplifier is set by 10 Ω resistor as shown in Fig. 3.7.

3.6 Low-pass filter

Figure 3.8 shows the unity gain, first order low-pass filter consists of one capacitor and one variable resistor (1/4 AD5204). The filter can be selected or deselected by a SPDT switch, ADG333A. Its 3 dB bandwidth ($1/2\pi RC$) is easily changed by adjusting the digital potentiometer via 3-wire serial interface. As it is seen from the figure AD5204 has parasitic capacitances at its terminals. In the previous stage, CLC414 is used as a gain block. Direct capacitive loading on the output pin of CLC414 can lead to peaking in the frequency response, overshoot in the pulse response, ringing or even oscillations. Capacitive loads greater than 5 pF should be buffered by connecting a small resistance usually, 10 Ω to 50 Ω, in series with the output. The resistor R_s is used for this purpose.

The maximum value of the cutoff frequency of the filter is 721 kHz. It is determined by the code dependent bandwidth of AD5204. The code is the eight data bits transferred into the variable resistor latch which holds its programmed resistance value. The range of cutoff frequency of the filter is given by the fixed resistance of AD5204 (10 kΩ) divided by the sum of the wiper contact resistance (45 Ω) and R_s (25 Ω), i.e., $10^4/(45+25)$. That means if the upper value is 700 kHz, then the lower value is approximately 5 kHz. The capacitor value, C, is 3.2 nF for this range. In order to reduce the cutoff frequency below 5 kHz the capacitor value must be increased. Capacitor selection is very important for a high performance filter. Capacitor behavior can vary significantly from ideal, introducing series resistance and inductance. Recommended capacitor types are: NPO ceramic, silver mica, metallized polycarbonate, polystyrene, and polypropylene. We chose polypropylene capacitors which have wide capacitance range.

It is important to choose an op amp that can provide the necessary DC precision,

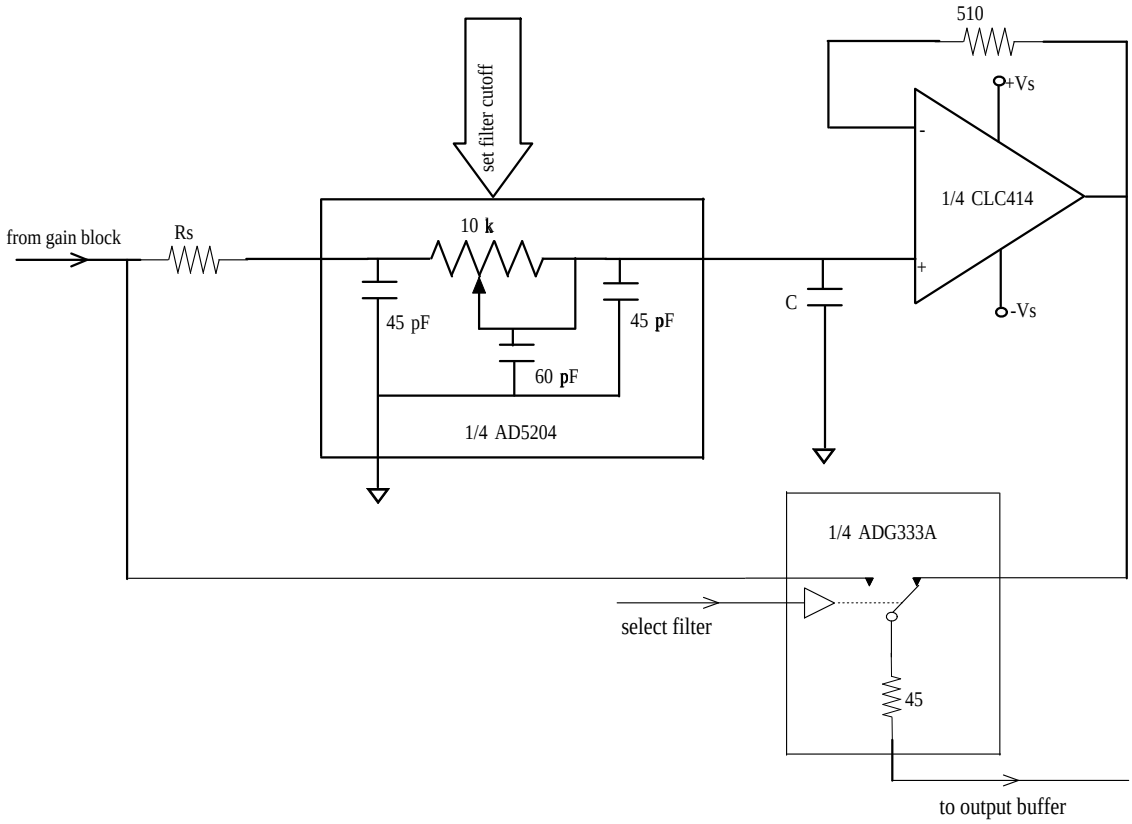

Figure 3.8: Low-pass filter.

noise, distortion, and speed. For a first order filter, op amp bandwidth should be at least 50 times the cutoff frequency. Therefore we need an op amp whose bandwidth is at least 35 MHz. The slew rate of the op amp must be greater than $\pi \times V_{op-p} \times filter\ bandwidth$. In our design, this becomes 11.5 V/μs. CLC414 satisfies these requirements exceedingly.

3.7 Control circuitry and parallel port interface

In order to control the digital lines of the DACs, switches, and digital potentiometers we need a computer interface to our system. Except for switches, these devices have 3-wire serial interface. At each clock (CLK) edge the data in the serial data input (SDI) line is pushed into the serial register in the device. After transferring all the address and data bits, load (LD) is activated and the data in the serial register is latched to the DAC register. Since only one device is activated at a time, the CLK and SDI lines can be combined together. However, each device needs its own LD line. The parallel port has 8 data, 4 control, and 5 status lines. Data can be written to data and control lines and can be read from status lines. We have to control more than 12 LD lines. Therefore we need a decoding circuitry which is shown in Fig. 3.9.

XC4005XL [27], low-voltage field programmable gate array (FPGA), contains 5,000 logic gates. Inputs on the XC4005XL are both TTL and 3.3 V CMOS compatible. It has 77 user i/o pins. It has an advantage that its configuration can be changed easily. An FPGA includes configurable logic blocks and input/ouput blocks which provide the functional elements and the interface between package pins and internal signal lines. The functionality of each block is customized by loading configuration data into internal memory cells. The FPGA can either actively read its configuration data from an external serial PROM, or the configuration data can be written into the FPGA from an external device.

We provided six jumpers (JMP1-JMP6) on the board to select the configuration

mode of the FPGA. It can be programmed both from the paralel port and external serial EEPROM. AT17C256 [28] is a cost-effective configuration memory for FPGA. XC17256EL [27] can also be used for this purpose, but it can be programmed only once. When power is applied to an FPGA, an internal circuit forces initialization of the configuration logic. The configuration mode pins M0, M1, and M2 determine the configuration mode. By tying these pins to ground with JMP2, the master serial mode is selected. The FPGA CCLK output drives the CLK input of the AT17C256 via JMP3. Its DIN input receives the configuration data in serial form from the DATA output of the configurator via JMP4. JMP1 is used to provide either 5 V or 3.3 V to the serial EEPROM. Slave serial mode can be selected by disconnecting JMP2. Vpp input of the EEPROM is connected to ground via JMP6. In slave serial mode, parallel port configures the FPGA with control lines connected to the PROGRAM, DIN, and CCLK inputs via JMP5, JMP4, and JMP3. Care must be taken not to force the chip into an undesired boundary scan state by inadvertently applying boundary scan input patterns to TMS, TCK, and TDI pins. In order to prevent this we connected TCK and TDI pins to ground with 4.7k ohm pull down resistors.

After programming the FPGA, the desired bit sequence is sent to the FPGA's user programmable i/o pins via data lines of the parallel port. While sending address and data bits, timing requirements of the ICs must be satisfied. An algorithm shown below is developed to program the DACs or to control the switches. Pin assignments of parallel port and XC4005XL is given in Appendix C.

- Initial state; parallel port data register is cleared.

- Address and data bits of target IC is obtained from an external input (not necessary for switches).

- Parallel bit sequence is sent from 9 to 4 DB25 pins of parallel port. Internal decoder enables only one LD line.

• One bit at a time is sent from pin 2 when the pin 10 indicates that internal clock signal is low (not necessary for switches).

• After sending all the address and data bits, pin 3 is strobed high or low to load the data into IC register. While this is done, clock signal is cancelled with pin 16. For the switches, pin 3 sends either a pulse or a high/low logic signal.

• Parallel port data register is cleared. The above steps are repeated for other channels.

As it is seen from Fig. 3.9 we have two grounds. The digital ground which parallel port is connected to is often noisy and should be isolated from the analog ground. HCPL-0721 [29] is used for this purpose. On power up ADM809 [23] produces a low level pulse to provide a reset signal to the DACs.

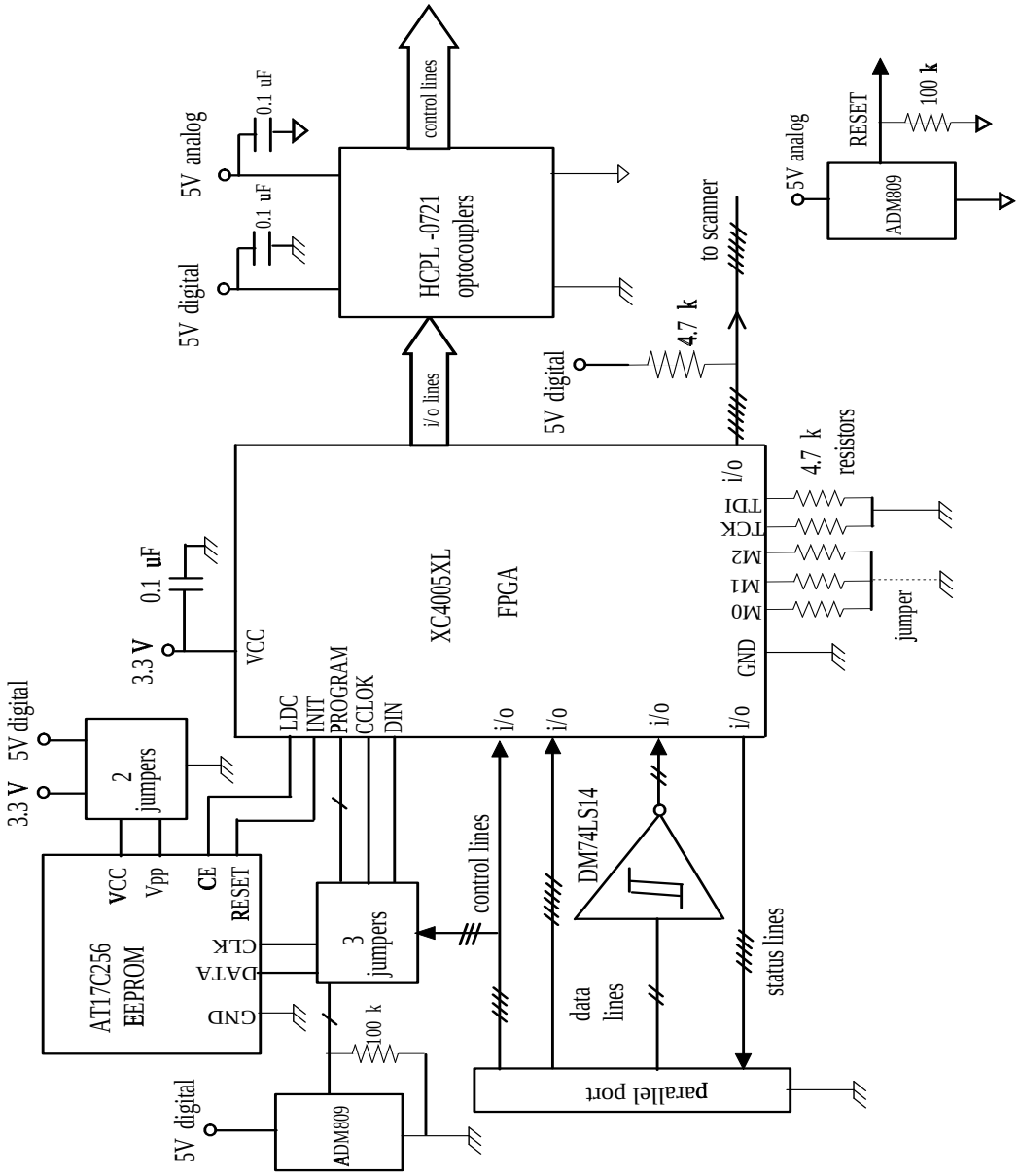

Figure 3.9: Control circuitry.

Chapter 4

CONCLUSION

In this thesis, we presented a detailed description of an electronic system which is used to drive 32 cantilevers. The design is suitable to operate the AFM in constant force or constant height contact mode. The operation of contact mode AFM can be summarized as follows: sample is scanned, and the deflection of the cantilever is detected by a sensor and is converted to an electrical signal by a transducer. It is then amplified and used as feedback and data signal. The piezoresistive detection scheme is employed in our system because it is very suitable for parallel operation and does not need any external component like a laser. Parallel operation increases the throughput of the AFM system. In this way large samples are imaged faster.

By operating three boards in parallel we will able to drive 96 cantilevers. Each channel has its own sensor and actuator. These are connected with connectors to our board. Each channel has its own analog circuitry and shares a common controller. Operating parameters, gain, bias voltage, etc., are set via parallel port before the operation. The overall circuitry consists of several blocks. While designing each block we try to minimize the size of the PCB. Therefore highly integrated circuits, e.g., quad op amps, are preferred while selecting the components. Also we try to minimize the number of control lines of

DACs, potentiometers, and switches. The surface mount chip capacitors and resistors are mostly used. The SOIC package ICs are preferred to use both sides of the PCB and to reduce any parasitic capacitance between the device pins. We also use four power planes for optimum performance. We place the components on the board such that the routing tracks would be as short as possible. This also reduces the crosstalk between mutiple signals. Since the resolution is determined by noise we try to minimize the noise in the first stage of the amplifiers. We also placed bypass capacitors very close to the supply pins of the ICs. The other amplifiers have wide bandwidth in order not to introduce too much phase shift. The slew rate of the high voltage amplifiers has an important effect on AFM images. We used very high slew rate power amplifiers to drive the actuator. The analog ouput signal is filtered and buffered at the last stage.

We also analyzed the steady state tip sample interaction in AFM by using an electrical circuit simulator. The phase shift between the cantilever excitation and tip, and the amplitude versus distance curves are obtained with sample stifness as a parameter. The height shifts and hysteresis in amplitude and phase curves are observed as a result of the influence of the force between tip and sample. The damping and switching mechanisms are explained using the force traces obtained from simulations. The oscillation amplitude dependence of operating mode is inspected. We find that improper selection of the free tip oscillation amplitude is the cause of operating state transitions.

Appendix A

PCB Layout

PCB layout of all layers, the top, and the bottom sides are shown in the following pages.

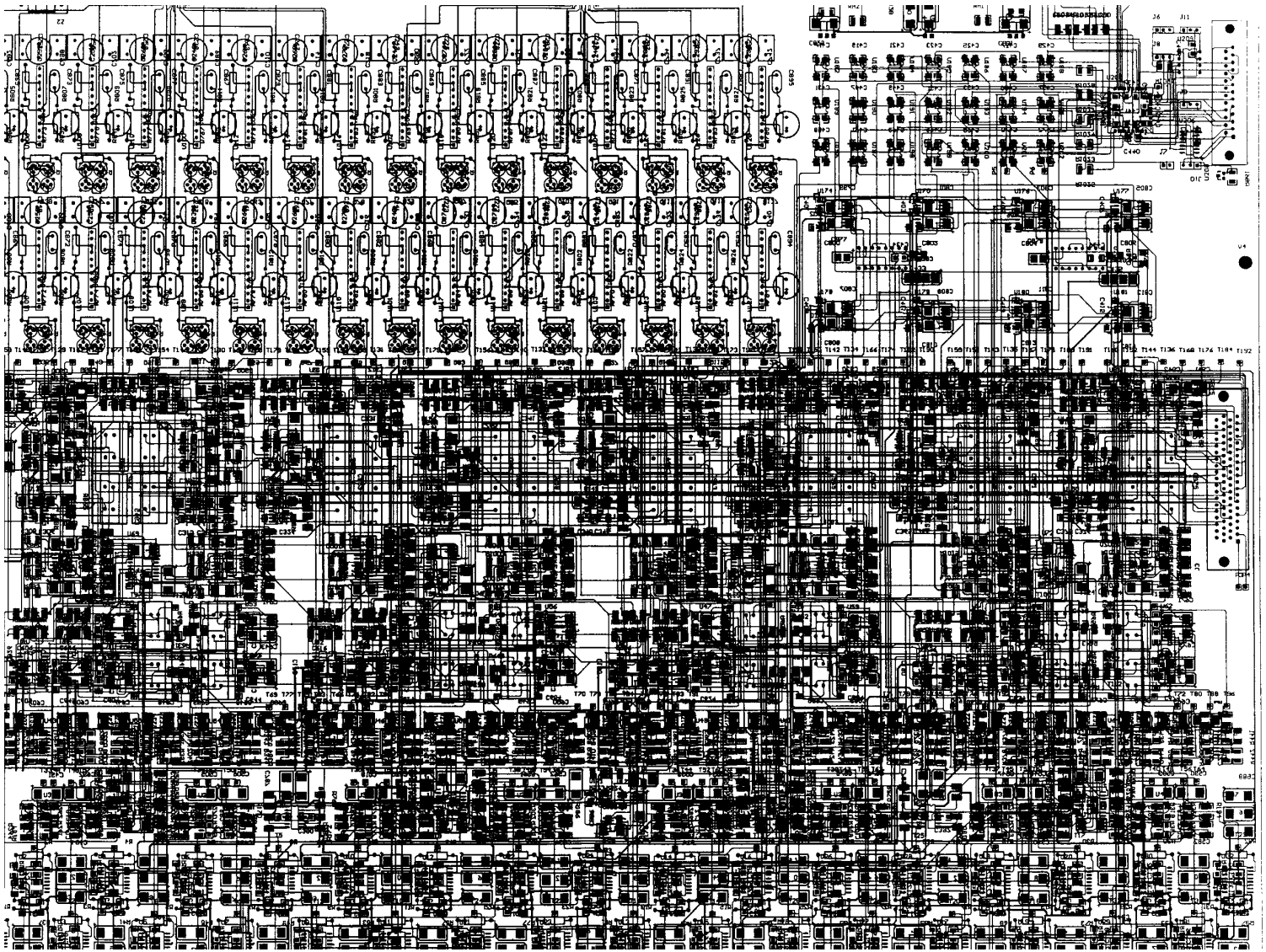

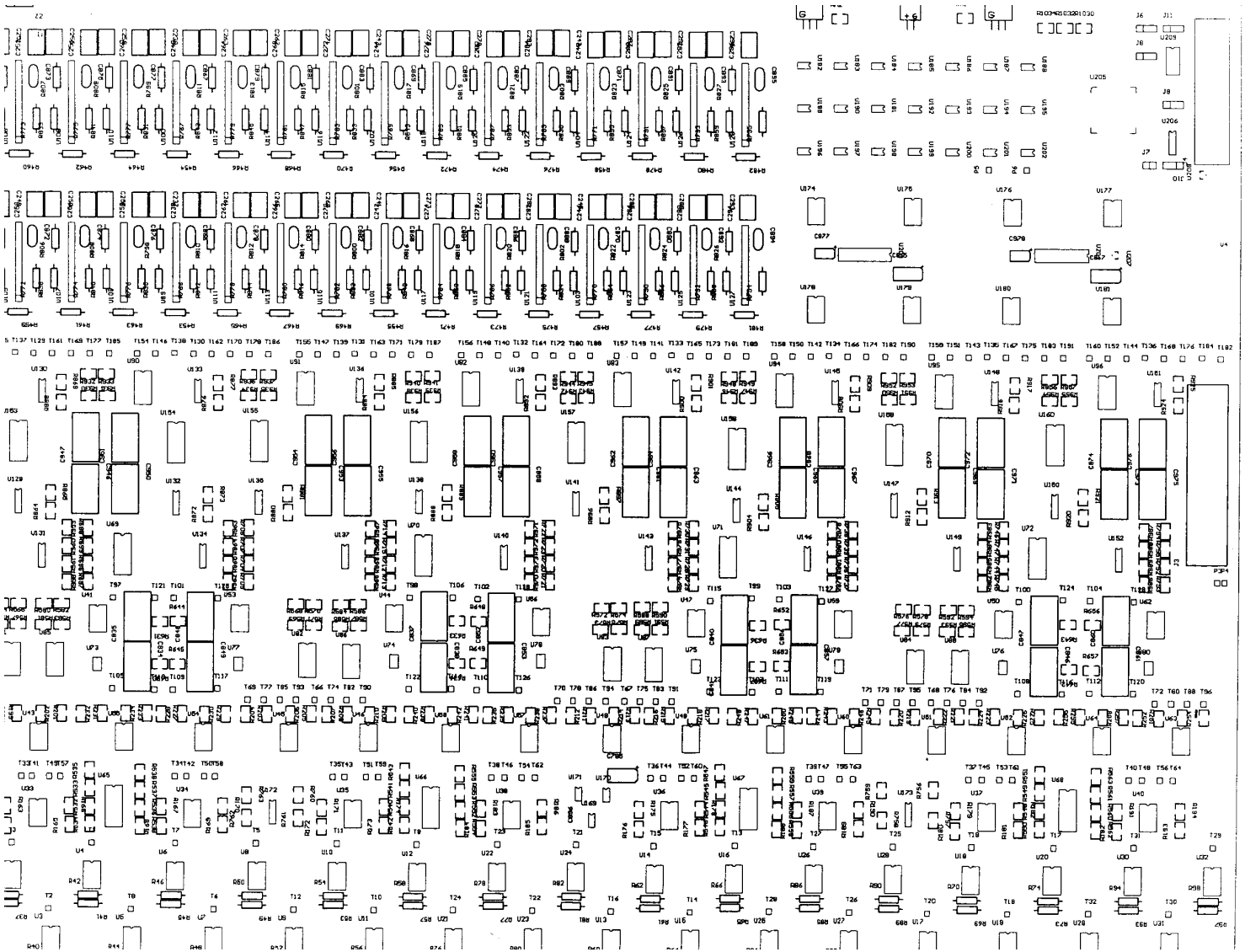

Appendix B

Component List

Part number	Quantity	Description
AD5204BR10	16	IC (SOIC pkg)
AD588BQ	2	IC (CERDIP pkg)
ADG333ABR	16	IC (SOIC pkg)
ADG662BRU	8	IC (TSSOP pkg)
ADM809RART	2	IC (SOT-23 pkg)
AT17C256-10PC	1	IC (DIP pkg)
CLC414AJE	24	IC (SOIC pkg)
DAC8043UC	1	IC (SOIC pkg)
DAC8420ES	8	IC (SOIC pkg)
DAC8840FS	8	IC (SOIC pkg)
DM74LS14M	1	IC (SOIC pkg)
HCPL-0721	21	optoisolator (SOIC pkg)
LM1085IT-5.0	1	regulator (TO-220 pkg)
LM1086IT-3.3	1	regulator (TO-220 pkg)
LM317T	1	regulator (TO-220 pkg)
LM2990T-5.0	1	regulator (TO-220 pkg)
LM1086IT-5.0	1	regulator (TO-220 pkg)
LM2990T-15	1	regulator (TO-220 pkg)
LM837M	2	IC (SOIC pkg)

OP467GS	32	IC (SOIC pkg)
OPA2107AU	1	IC (SOIC pkg)
PA98	32	IC (SIP03 pkg)
SSM2017S	32	IC (SOIC pkg)
XC4005XL	1	IC (VQ100 pkg)
REF02BU	1	IC (SOIC pkg)
MICTOR	4	connector (767054-1)
2N4416	128	jfet (TO-72 pkg)
2EZ150D5	2	zener, 150V, axial
1.8 kΩ	96	thick film chip, 1/4 W, 1%, 1210
10 Ω	34	thick film chip, 1/4 W, 1%, 1210
10 Ω	32	metal film, 1/4 W, 1%, axial
100 Ω	32	metal film, 1/4 W, 1%, axial
100 kΩ	34	thick film chip, 1/4 W, 1%, 1210
100 kΩ	32	metal film, 1/4 W, 1%, axial
10 kΩ	280	thick film chip, 1/4 W, 1%, 1210
10 kΩ	32	metal film, 1/4 W, 1%, axial
150 kΩ	96	thick film chip, 1/4 W, 1%, 1210
1 kΩ	108	thick film chip, 1/4 W, 1%, 1210
2.4 kΩ	1	thick film chip, 1/4 W, 1%, 1210
220 Ω	3	thick film chip, 1/4 W, 1%, 1210
24 Ω	32	thick film chip, 1/4 W, 1%, 1210
270 Ω	3	thick film chip, 1/4 W, 1%, 1210
300 Ω	33	thick film chip, 1/4 W, 1%, 1210
4.7 kΩ	15	thick film chip, 1/4 W, 1%, 1210
47 kΩ	96	thick film chip, 1/4 W, 1%, 1210
510 Ω	64	thick film chip, 1/4 W, 1%, 1210
560 kΩ	32	thick film chip, 1/4 W, 1%, 1210
100 Ω	32	thick film chip, 1/4 W, 1%, 1210
20 kΩ	32	thick film chip, 1/4 W, 1%, 1210
30 kΩ	32	thick film chip, 1/4 W, 1%, 1210
330 Ω	32	metal film, 1/4 W, 1%, axial
3 kΩ	64	metal film, 1/4 W, 1%, axial

10 μF	289	tantalum electrolytic chip, 25V, 20%
6.8 μF	48	tantalum electrolytic chip, 25V, 20%
1 μF	2	tantalum electrolytic chip, 25V, 20%
0.1 μF	414	ceramic chip, 25V, 10%, 1206
10 pF	1	ceramic chip, 50V, 0.5%, 0402
0.1 nF	64	polypropylene, 50V, 5%, radial
0.27 nF	64	polypropylene, 50V, 5%, radial
0.68 nF	64	polypropylene, 50V, 5%, radial
1.8 nF	64	polypropylene, 50V, 2%, radial
4.7 nF	64	polypropylene, 50V, 2%, radial
12 nF	64	polypropylene, 50V, 2%, radial
22 nF	64	polypropylene, 50V, 2%, radial
33 nF	64	polypropylene, 50V, 2%, radial
68 nF	64	polypropylene, 50V, 2%, radial
150 nF	64	polypropylene, 50V, 2%, radial
10 pF	1	NPO, 500V, $\pm$0.5 pF, radial
10 μF	64	aluminum electrolytic, 250V, 20%, radial
0.1 μF	64	metallized polyester, 250V, 10%, radial

Table B.1: Component list

Appendix C

Pin assignments of parallel port

Pins 2, 3, and 14 are inverted with a schmitt trigger inverter.

DB25 pin	Register bit	Usage	XC4005XL pin
2	D0	SDI line	41
3	D1	LD line	42
4	D2	decoder input	43
5	D3	decoder input	44
6	D4	decoder input	45
7	D5	decoder input	46
8	D6	decoder input	47
9	D7	decoder input	56
15	S3	unused	59
13	S4	unused	60
12	S5	unused	62
10	S6	clock read	67
11	S7	unused	69
1	C0	configuration	52
14	C1	configuration	74
16	C2	clock inhibitor	84
17	C3	configuration	72
18-25	GND	GND	GND

Table C.1: Pin assignments of parallel port

Bibliography

[1] G. Binning, C. F. Quate, and C. Gerber, "Atomic force microscope," *Phys. Rev. Lett.*, vol. 56, no. 9, pp. 930–933, 1986.

[2] M. Tortonese, R. C. Barrett, and C. F. Quate, "Atomic resolution with an atomic force microscope using piezoresistive detection," *Appl. Phys. Lett.*, vol. 62, no. 8, pp. 834–836, 1993.

[3] S. C. Minne, S. R. Manalis, and C. F. Quate, "Parallel atomic force microscopy using cantilevers with integrated piezoresistive sensors and integrated piezoelectric actuators," *Appl. Phys. Lett.*, vol. 67, no. 26, pp. 3918–3920, 1995.

[4] S. R. Manalis, S. C. Minne, and C. F. Quate, "Atomic force microscopy for high speed imaging using cantilevers with an integrated actuator and sensor," *Appl. Phys. Lett.*, vol. 68, no. 6, pp. 871–873, 1996.

[5] S. R. Manalis, S. C. Minne, A. Atalar, and C. F. Quate, "High-speed atomic force microscopy using an integrated actuator and optical lever detection," *Rev. Sci. Instrum.*, vol. 67, no. 9, pp. 3294–3297, 1996.

[6] S. C. Minne, G. Yaralıoğlu, S. R. Manalis, J. D. Adams, J. Zesch, A. Atalar, and C. F. Quate, "Automated parallel high-speed atomic force microscopy," *Appl. Phys. Lett.*, vol. 72, no. 18, pp. 2340–2342, 1998.

[7] S. C. Minne, J. D. Adams, G. Yaralıoğlu, S. R. Manalis, A. Atalar, and C. F. Quate, "Centimeter scale atomic force microscope imaging and lithography," *Appl. Phys. Lett.*, vol. 73, no. 12, pp. 1742–1744, 1998.

[8] J. L. Hutter and J. Bechhoefer, "Manipulation of van der waals forces to improve image resolution in atomic force microscopy," *J. Appl. Phys.*, vol. 73, no. 9, pp. 4123–4129, 1993.

[9] U. Hartmann, "van der waals interactions between sharp probes and flat sample surfaces," *Phys. Rev. B.*, vol. 43, no. 3, pp. 2404–2407, 1991.

[10] P. J. de Pablo, J. Colchero, M. Luna, J. Gómez-Herrero, and A. M. Baró, "Tip-sample interaction in tapping-mode scanning force microscopy," *Phys. Rev. B.*, vol. 61, no. 20, pp. 14179–14183, 2000.

[11] R. García and A. S. Paulo, "Dynamics of a vibrating tip near or in intermittent contact with a surface," *Phys. Rev. B.*, vol. 61, no. 20, pp. 13381–13384, 2000.

[12] B. Anczykowski, D. Kruger, K. L. Babcock, and H. Fuchs, "Basic properties of dynamic force spectroscopy with the scanning force microscope in experiment and simulation," *Ultramicroscopy*, vol. 66, pp. 251–259, 1996.

[13] A. Kuhle, A. H. Sorensen, J. B. Zandbergen, and J. Bohr, "Contrast artifacts in tapping tip atamic force microscopy," *Appl. Phys. A*, vol. 66, pp. S329–S332, 1998.

[14] M. Hoummady, E. Rochat, and E. Farnault, "Nonlinear tip-sample interactions affecting frequency responses of microcantilevers in tapping mode atomic force microscopy," *Appl. Phys. A*, vol. 66, pp. S935–S938, 1998.

[15] O. Sahin and A. Atalar, "Analysis of tip-sample interaction in tapping-mode atomic force microscope using an electrical circuit simulator," *Appl. Phys. Lett.*, vol. 78, pp. 2973–2976, 2001.

[16] C. Argento and R. H. French, "Parametric tip model and force-distance relation for hamaker constant determination from atomic force microscopy," *J. Appl. Phys.*, vol. 80, no. 11, pp. 6081–6090, 1996.

[17] R. G. Winkler, J. P. Spatz, S. Sheiko, M. Moller, P. Reineker, and O. Marti, "Imaging material properties by resonant tapping-force microscopy : A model investigation," *Phys. Rev. B*, vol. 54, no. 12, pp. 8908–8912, 1996.

[18] P. Gleyzes, P. K. Kuo, and A. C. Boccara, "Bistable behavior of a vibrating tip near a solid surface," *Appl. Phys. Lett.*, vol. 58, no. 25, pp. 2989–2991, 1991.

[19] A. Kuhle, A. H. Sorensen, and J. Bohr, "Role of attractive forces in tapping tip force microscopy," *J. Appl. Phys.*, vol. 81, no. 10, pp. 6562–6569, 1997.

[20] G. G. Yaralıoğlu, *Noise Analysis of Interdigital Cantilevers for Atomic Force Microscopy.* PhD thesis, Department of Electrical and Electronics Engineering, Bilkent University, October 1998.

[21] www.amp.com

[22] www.ics-ltd.com

[23] www.analog.com

[24] www.national.com

[25] www.burr-brown.com

[26] www.apexmicrotech.com

[27] www.xilinx.com

[28] www.atmel.com

[29] www.hp.com